DTIC FILE COPY

(2)

AD-A206 072

AFOSR.TR. 89-0366

20030203014

ARPA 6155

Program Code 7410

Program Title
Environmental Effects in Niobium
Base Alloys and Other Selected
Intermetallic Compounds

Sponsored by
Defense Advanced Research Projects Agency
DARPA Order No. 6155

Monitored by AFOSR Under Contract No. F49620-88-C-0013

Contractors
Department of Materials Science and Engineering
University of Pittsburgh

Department of Metallurgical Engineering and Materials Science
Carnegie Mellon University

Principal Investigators

G. H. Meier
412-624-9741
University of Pittsburgh

A. Thompson
412-268-2700
Carnegie Mellon University

Period Covered
November 1, 1987 - October 31, 1988

First Annual Report
December 15, 1988

89 [illegible]

SECURITY CLASSIFICATION OF THIS PAGE

REPORT DOCUMENTATION PAGE

Form Approved
OMB No. 0704-0188

1a. REPORT SECURITY CLASSIFICATION UNCLASSIFIED

1b. RESTRICTIVE MARKINGS

2a. SECURITY CLASSIFICATION AUTHORITY

2b. DECLASSIFICATION / DOWNGRADING SCHEDULE

3. DISTRIBUTION / AVAILABILITY OF REPORT
UNCLASSIFIED/UNLIMITED

4. PERFORMING ORGANIZATION REPORT NUMBER(S)

5. MONITORING ORGANIZATION REPORT NUMBER(S)
AFOSR-TR- 89-0366

6a. NAME OF PERFORMING ORGANIZATION
Dept. of Materials Science
Engineering, Univ. of Pittsburgh

6b. OFFICE SYMBOL *(If applicable)*

7a. NAME OF MONITORING ORGANIZATION
Air Force Office of Scientific
Research /NE

6c. ADDRESS *(City, State, and ZIP Code)*
848 Benedum Hall
Pittsburgh, PA 15261

7b. ADDRESS *(City, State, and ZIP Code)*
Bolling AFB
Washington, DC 20332

8a. NAME OF FUNDING / SPONSORING ORGANIZATION ~~Defense Advanced Research Projects Agency~~ AFOSR

8b. OFFICE SYMBOL *(If applicable)* NE

9. PROCUREMENT INSTRUMENT IDENTIFICATION NUMBER
F49620-88-C-0013

8c. ADDRESS *(City, State, and ZIP Code)*
~~1400 Wilson Boulevard~~ BLDG 410
~~Arlington, VA 22209-2308~~ BAFB, DC 20332

10. SOURCE OF FUNDING NUMBERS

PROGRAM ELEMENT NO.	PROJECT NO.	TASK NO.	WORK UNIT ACCESSION NO.
61102F	DARPA		

11. TITLE *(Include Security Classification)*
Environmental Effects in Niobium Base Alloys and Other Selected Intermetallic Compounds

12. PERSONAL AUTHOR(S)
Meier, G. H., Univ. Of Pittsburgh and Thompson, A. W., Carnegie Mellon University

13a. TYPE OF REPORT
First Annual

13b. TIME COVERED
FROM 11/1/87 TO 10/31/88

14. DATE OF REPORT *(Year, Month, Day)*
Dec. 15, 1988

15. PAGE COUNT
66

16. SUPPLEMENTARY NOTATION

17. COSATI CODES

FIELD	GROUP	SUB-GROUP
/		

18. SUBJECT TERMS *(Continue on reverse if necessary and identify by block number)*
Niobium Base Alloys, Intermetallics, Oxidation, Hydrogen, Mechanical Properties

19. ABSTRACT *(Continue on reverse if necessary and identify by block number)* (Aluminum Oxide) (Silicon dioxide)

Niobium aluminides and silicides as well as other intermetallic compounds have potential for use in advanced gas turbines where increased operating temperatures are necessary to obtain the targeted performance goals. These materials will be subjected to a variety of environments over a range of temperatures. Two of the principal reactants in these environments are oxygen and hydrogen. This program is concerned with the effects of oxygen and hydrogen on niobium alloys and other selected intermetallic compounds.

This program consists of two parts. Part I involves the effects of oxygen and is being performed at the University of Pittsburgh by Professors G. H. Meier and F. S. Pettit. Part II is being performed at Carnegie Mellon University by Professor A. W. Thompson.

The investigations involving oxygen are directed toward describing the conditions which must be achieved in order to have a continuous, protective Al_2O_3 or SiO_2 scale developed on niobium-base alloys and compounds, and other selected intermetallics, at temperatures between 600 and 1400°C. The studies concerned with hydrogen effects are directed toward determining solubility limits, hydrogen uptake and permeation rates, and the degree to which hydrogen degrades the mechanical properties of these materials. (AW)

20. DISTRIBUTION / AVAILABILITY OF ABSTRACT
☒ UNCLASSIFIED/UNLIMITED ☐ SAME AS RPT ☐ DTIC USERS

21. ABSTRACT SECURITY CLASSIFICATION
UNCLASSIFIED

22a. NAME OF RESPONSIBLE INDIVIDUAL
Rosenstein

22b. TELEPHONE *(Include Area Code)*
(202) 767-4933

22c. OFFICE SYMBOL
NE

DD Form 1473, JUN 86 *Previous editions are obsolete.* SECURITY CLASSIFICATION OF THIS PAGE

ARPA 6155

Program Code 7410

Program Title
Environmental Effects in Niobium Base Alloys and Other Selected Intermetallic Compounds

Sponsored by
Defense Advanced Research Projects Agency
DARPA Order No. 6155

Monitored by AFOSR Under Contract No. F49620-88-C-0013

Contractors
Department of Materials Science and Engineering
University of Pittsburgh

Department of Metallurgical Engineering and Materials Science
Carnegie Mellon University

Principal Investigators

G. H. Meier
412-624-9741
University of Pittsburgh

A. Thompson
412-268-2700
Carnegie Mellon University

Period Covered
November 1, 1987 - October 31, 1988

First Annual Report
December 15, 1988

Summary

Niobium aluminides and silicides as well as other intermetallic compounds have potential for use in advanced gas turbines where increased operating temperatures are necessary to obtain the targeted performance goals. These materials will be subjected to a variety of environments over a range of temperatures. Two of the principal reactants in these environments are oxygen and hydrogen. This program is concerned with the effects of oxygen and hydrogen on niobium alloys and other selected intermetallic compounds.

This program consists of two parts. Part I involves the effects of oxygen and is being performed at the University of Pittsburgh by Professors G. H. Meier and F. S. Pettit. Part II is being performed at Carnegie Mellon University by Professor A. W. Thompson.

The investigations involving oxygen are directed toward describing the conditions which must be achieved in order to have a continuous, protective Al_2O_3 or SiO_2 scale developed on niobium-base alloys and compounds, and other selected intermetallics, at temperatures between 600 and 1400°C. The studies concerned with hydrogen effects are directed toward determining solubility limits, hydrogen uptake and permeation rates, and the degree to which hydrogen degrades the mechanical properties of these materials.

PART I

OXIDATION OF NIOBIUM - BASE ALLOYS AND OTHER SELECTED INTERMETALLICS

by

R. R. Cerchiara, E. A. Gulbransen, F. S. Pettit and G. H. Meier

Department of Materials Science and Engineering
University of Pittsburgh

Oxidation of Niobium-Base Alloys and Other Selected Intermetallics

by

R. R. Cerchiara, E. A. Gulbransen, F. S. Pettit, and G. H. Meier
Department of Materials Science and Engineering
University of Pittsburgh

INTRODUCTION

Intermetallic compounds are currently being considered for a variety of high temperature applications because they offer a possible combination of creep resistance and low density which is superior to that provided by state-of-the-art, coated, superalloys. However, the achievement of adequate oxidation resistance in the systems which possess high specific strengths is a matter of concern. Figure 1 indicates some of the systems with potential for meeting these requirements. The purpose of this section is to describe the current understanding of alloy oxidation with particular emphasis on intermetallic compounds such as those listed in Figure 1. The mechanisms of oxidation will be treated in detail with review of specific data being used only to illustrate aspects of the mechanisms. The reader is directed to the excellent review by Aitken(1) for details of work prior to 1967.

The development of oxidation resistance in alloys is based on the addition of an element which will oxidize selectively and produce a protective surface oxide. The formation of this surface layer requires that the oxide be more stable than the lowest oxide of the base metal. Figure 2 indicates the free energies of formation of a few selected oxides. The oxides Al_2O_3, SiO_2, and BeO are of principal interest because they exhibit low diffusivities for both cations and anions as well as being highly stable. Thus the addition of Al to Ni, as in the case of aluminide coatings on nickel-base alloys, or Si to Mo, as in the case of $MoSi_2$ heating elements, clearly satisfy the stability requirements. However, in the case of Nb-, Ti-, or Zr-base alloys the oxides of the base metal are nearly as stable as those of Al, Si, or Be. A second requirement is that the concentration of the element added for oxidation resistance is sufficient for the formation of its oxide as an external layer rather than as internal precipitates. The two possibilities for the simple case where the oxygen partial pressure is too low to oxidize the base metal are illustrated in Figure 3. Alloys with low solute concentrations allow inward diffusion of oxygen which results in internal oxidation, Fig. 3a., while for high solute contents the outward diffusion of solute results in the formation of a continuous external layer of oxide, Fig. 3b. The critical solute concentration for the transition from internal to external oxidation has been expressed by Wagner(3) as

$$N_B^* = \left(\frac{\pi g^* N_0 D_0 V_M}{2 D_B V_{OX}}\right)^{1/2} \qquad (1)$$

Here N_0D_0 is the oxygen permeability in A, D_B is the solute diffusivity, g^* is a factor determined by the volume fraction of oxide required for the transition(often near 0.3), and V_M and V_{OX} are the molar volumes of the alloy and oxide, respectively. The solute content required for external scale formation is seen to increase with the solubility and diffusivity of oxygen and decrease with an increase in the solute diffusivity in the alloy. However, for most systems of interest, the oxide of the base metal can also form in the ambient atmosphere and grows until the more stable oxide of the solute B becomes continuous and stops the growth of the "transient oxide". This situation is illustrated schematically in Figure 4. The effect of transient oxidation on the transition from internal to external oxidation of B has been analyzed by Gesmundo and Viani(4) who found that an excess of solute above that predicted by equation 1 is required in the presence of transient oxides. The amount of excess solute required is predicted to increase as the growth rate of the transient oxide increases. The conditions assumed in the derivation of equation (1) do not apply rigorously to the oxidation of intermetallics for several reasons which will become apparent. Nevertheless, the above analysis provides a useful qualitative method to evaluate the effects of variables such as temperature, composition, and atmosphere on the selective oxidation process.

Figure 5 illustrates schematically for $MoSi_2$ a feature common to oxidation of intermetallic compounds with small homogeneity ranges. Here the removal of Si to form a layer of SiO_2 immediately results in the formation of a layer of the next lower silicide, Mo_5Si_3, adjacent to the oxide. This situation, which is in contrast to the smooth concentration gradient in the alloy depicted in Figure 4(b), means that the properties of the lower compound determine the ability of the alloy to maintain the growth of the protective oxide. Apparently Mo_5Si_3 provides a sufficient flux of Si to the oxide/alloy interface to maintain the growth of a silica layer. This is not the case, however, with many intermetallic compounds and represents a major difference between the oxidation of intermetallic compounds and solid solutions.

Effects of Temperature

The effect of temperature on the selective oxidation process is determined by the temperature dependence of all of the terms in equation 1 and that of the growth rate of the transient oxides. Figure 6, from the work of Pettit(6), shows the temperature dependence of the transition from internal to external formation of alumina on Ni-Al alloys. These alloys, which include solid solutions and the compound Ni_3Al, are characterized by three regions: (I) 0-10at%Al, internal Al oxides under external NiO external scales result; (II) 10-30at%Al, external Al_2O_3 forms but cannot be sustained because of an inadequate supply of Al and is overgrown by mixed Ni-Al scales; and (III) >30at%Al, the external Al_2O_3 is maintained by a sufficient supply of Al. Regions II and III both extend to lower Al contents as the temperature is increased. This type of behavior is generally explained in terms of more rapid diffusion of solute in the alloy at higher temperatures which provides a greater flux to the surface to develop and maintain the protective scale. This phenomenon is not universal, however. The cross-hatched region in Figure 7 indicates the temperatures and compositions where the compound TiAl develops an external Al_2O_3 scale in pure oxygen. In this case, for a given Al content, external alumina formation is promoted at low temperature(7).

An effect of temperature which is peculiar to intermetallic compounds is the tendency of some of them to undergo a form of attack at intermediate temperatures, usually less than 1000°C, which results in disintegration of the alloy. This disintegration was first studied for $MoSi_2$ by Fitzer(8) who termed it "pesting". The pest effect has been studied most extensively for $MoSi_2$, particularly by Berkowitz and coworkers(9), but data compiled by Aitken(1), indicates its occurrence in a wide range of intermetallic compounds. The basic characteristics of the pest effect may be summarized as follows:

1. Attack is predominantly intergranular, often associated with grain boundary hardening.
2. Exposure to a reactive gas, particularly O_2, is required.
3. Rapid attack is preceded by an incubation period.
4. Disintegration occurs over a limited temperature range which varies from one compound to the next.
5. Some compounds appear to be immune.
6. The detailed mechanism is still not fully understood.

Improved understanding of the "pest" mechanism should be achievable by incorporating techniques such as acoustic emission measurements, modern surface analysis, and TEM/STEM into studies using more conventional techniques.

The effect of temperature cycling can also have substantial effects on the selective oxidation process. Figure 8 is a schematic comparison between isothermal and cyclic oxidation which is valid for many alloy systems. The rates are comparable for short times but scale spalling caused by thermal stresses which result from the thermal expansion mismatch between the oxide and alloy and which become larger as the scale thickens eventually produces weight losses. The amount of degradation under cyclic conditions generally is substantially greater than under isothermal conditions. Cyclic oxidation data for intermetallic compounds are limited but those available for NiAl in diffusion aluminide coatings on Ni-base alloys(10), Fe-silicides(11), and Ni-silicides(12) indicate similar behavior to that in Figure 8. Typical cyclic oxidation data for a range of Ni-silicides are presented in Figure 9.

Effects of Alloying Elements

The beneficial effects of third element additions on the selective oxidation process are best typified by additions of Cr to Ni-Al alloys which promote external Al_2O_3 scale formation at substantially lower Al contents than those indicated in Figure 6. The effects of Cr additions are summarized in the isothermal(13,14) and cyclic(15) oxidation maps in Figure 10. The explanation of these effects requires consideration of the influence of Cr on all of the parameters in equation 1. and on the growth rate of the transient oxide. The predominant effect of Cr is generally thought to involve reduction of the oxygen solubility, N_0, but other factors must be important. For example, Si additions to Ni-Al alloys, which should decrease N_0 in a similar manner to Cr, actually retards the development of external Al_2O_3 scales for certain ranges of Al contents(16). The cause of this retardation appears to be associated with Si stabilizing phases in which Al diffusion is slower. Regardless of the exact mechanism, these data indicate the need to consider all of the important parameters in analyzing third element effects. Again, data for most intermetallic compounds are lacking but Cr and V additions to Ti-aluminides(17) and Ti and Cr additions to Nb-aluminides(18,19) have been shown to promote external Al_2O_3 scale formation at much lower Al contents than those required for the binary alloys.

Additional effects of alloying involve changes in the melting points of the alloys and the oxide scales which form on them. For example, Figure 1 indicates that the amount of alloying elements required to produce the Nb-Ti-Cr-V-Al alloys, which are marginal alumina formers(19), has lowered the melting point well below that of binary NiAl. The melting temperature of the transient oxide scales which form on the alloys can also be greatly affected by alloying additions.

Effects of Atmosphere Composition

The pressure and composition of the reactive gas atmosphere can have substantial effects on the oxidation behavior of many intermetallic compounds. Figure 11, taken from the work of Perkins and Packer(20), shows the effect of oxygen partial pressure on the formation of continuous silica films on $MoSi_2$ as a function of temperature. The silica film forms in an intermediate pressure range at each temperature. This type of behavior may be understood by considering both the condensed and vapor species for the Mo-O and Si-O systems. The "active" oxidation at high oxygen pressures is associated with the formation of MoO_3 in the scales which grows rapidly, being liquid above 701°C, and prevents the formation of a continuous silica film. The "active" region at low oxygen pressures, which also occurs for pure Si(21), results from the high pressure of SiO over SiO_2 which leads to reactive volatilization of Si oxides rather than the formation of a protective film. The thermodynamic analysis of such phenomena will be treated in the next section of this report.

Additional effects of the atmosphere can occur if it contains a second reactive component, even the nitrogen in air. This effect is most striking for the oxidation of Ti-aluminides. Figure 7 indicated that protective alumina scales were formed on TiAl, exposed in oxygen, up to temperatures near 950°C. However, the same exposures conducted in air result in the formation of TiO_2-rich scales which grow at rates orders of magnitude faster than the alumina scales. This effect, which is discussed in more detail in reference (7), has been shown by Choudhury etal(22) to be associated with the presence of nitrogen as opposed to any other variable such as oxygen pressure. The detailed mechanisms of the effect of nitrogen and the extent that it applies to other intermetallic systems is in need of further study. Data for the reaction of intermetallic compounds in other mixed oxidants are rather limited except for a few studies in sulfidizing/oxidizing atmospheres associated with coal conversion atmospheres. Natesan(23,24) has reported severe sulfidation of Ni_3Al in these atmospheres while Kim and Meier(25) have found the silica scales formed on Ni- and Fe-silicides to be extremely resistant.

Specific Systems

Figure 12 presents an overview of the temperature to which alloy systems containing intermetallic phases can maintain reasonable oxidation resistance. This diagram, which has been updated from that published by Aitken(1) by the inclusion of data on Fe-Si and Ni-Si, is based on an approximate oxidation rate of 20 mg/cm^2 in 100 hours for the most oxidation resistant compound in each system. This representation obviously oversimplifies a very complex body of data but is useful for qualitative comparisons. The temperature ranges where breakdown phenomena, such as "pesting", have been reported are crosshatched in the Figure.

Summary

The basic concepts of selective oxidation apply to intermetallic compounds. However, the details of the selective oxidation process for the compounds of major interest for high temperature applications differ as a result of:

a. Generally lower diffusivities in the alloy
b. Lower interstitial solubilities.
c. Smaller differences in the stabilities of the oxides of the components.
d. Tight stoichiometry of many compounds.
e. Transient oxides which grow with linear or rapid parabolic kinetics.

Adequate solubility and diffusivity data are not available for most systems.

The effects of oxidation temperature and alloying on the selective oxidation process varies from one compound to the next depending on their relative effects on:

a. Solubility and diffusivity of interstitials.
b. Diffusivities of the metallic components.
c. Rate of transient oxidation.
d. Alloy phases stabilized.
e. Vaporization of metallic and oxide species.
f. Oxide and alloy melting.

The oxidation of some compounds is sensitive to the composition of the oxidizing atmosphere e.g. the presence of nitrogen.

CURRENT PROGRAM: RESULTS AND DISCUSSION

Figure 1 indicates a number of intermetallic alloys which are of potential interest with regard to their high temperature oxidation behavior. The compounds chosen for this study were limited to the aluminides and silicides of Nb, Ta, Mo, and Ti. Others, such as the Ni-aluminides, were eliminated because they have been extensively studied in other programs and the beryllides were eliminated because of safety considerations in preparing and handling the materials. The study consists of two efforts: a thermochemical analysis of the oxidation of intermetallic compounds and an experimental investigation of their oxidation mechanisms. These efforts are described in detail in the following.

Thermochemistry of the Condensed Phases and Volatile Species
in the Oxidation of Intermetallic Alloys
Containing Niobium, Silicon and Aluminum

Introduction

Thermochemistry is used to identify the condensed oxide phases, the oxygen potential of the reacting gases, the volatile metal and oxide species and the physical state of the oxide layer and volatilized oxide. Following the methods used in earlier studies (26,27) we will use standard Gibbs free energy data, ΔG_f^o, and equilibrium constants, log K_p, (28-30) to evaluate the condensed phases and the equilibrium pressures of the volatile species over the several condensed phases as a function of temperature and oxygen potential of the gas mixture. Log $p_{M_xO_y}$ vs. log p_{O_2} and log p_{H_2}/p_{H_2O} diagrams show the influence of the oxygen potential on the equilibrium pressure of the volatile species M_xO_y. To summarize the data log $p_{M_xO_y}$ vs. $\frac{1}{T}$ diagrams are used.

Table 1 shows a list of the condensed oxide phases for the metals Nb, Mo, Si and Al at 1250K together with the available melting and boiling temperatures.

Results

Figures 13-16 show log $p_{M_xO_y}$ vs log p_{O_2} and log p_{H_2}/p_{H_2O} diagrams for the four metals involved in the oxidation of the alloy systems Nb-Al and Mo-Si at 1250K. Log $p_{M_xO_y}$ is plotted on the left and log p_{O_2} on the bottom. Log p_{H_2}/p_{H_2O} values are plotted at the top of the diagram.

Figure 13 for the Nb-O system shows three oxides NbO, NbO_2 and N_2O_5 are formed. The equilibrium pressures of the four volatile metal and oxide species are shown in the diagram as a function of oxygen potential. Of particular interest are the equilibrium pressures at the oxygen interface, the metal-oxide interface and the inner oxide interface NbO-NbO_2.

In earlier studies (31) volatile species with log p below -9 have been shown to have negligible influence in the oxidation process. For log p = -9 to log p = -3 mixed oxidation and volatility can occur while for log p > -3 complete volatility is observed. The major volatile specie in the Nb - O system is NbO_2. Over the condensed phase NbO_2 log p_{NbO_2} = -14.2. At 1250K volatile species are not important for this system.

Figure 14 shows a log $p_{M_xO_y}$ vs log p_{O_2} diagram for the Mo-O system at 1250K. A very different diagram is observed. Two condensed phases are observed for 1250K MoO_2 and MoO_3. The latter phase is liquid above 1074K. Of special interest is the high equilibrium pressure of the vapor specie $(MoO_3)_3$ over $MoO_3(l)$ Here log p = -0.7 where p is in atmospheres. Complete volatility of the oxide occurs in the oxidation of Mo at 998K. Lower equilibrium pressures are found at the Mo-MoO_2 interface.

Figure 15 shows a log $p_{Si_xO_y}$ vs log p_{O_2} diagram for the Si-O system at 1250K. A new and different type of diagram is observed. Only one condensed phase, SiO_2, is observed in the oxidation of Si. SiO is the major volatile specie at 1250K with the maximum pressure occurring at the Si-SiO_2 interface. Here log $p_{SiO} = -5.6$. Very low pressures of SiO(g) occur at the SiO_2 - O_2 interface. For the oxidation of Si(s) at log $p_{O_2} = 0$ SiO can diffuse to cracks and defects in the oxide, react with O_2 and develop a coherent oxide film. For low O_2 pressure where log $p_{SiO} >$ log p_{O_2} rapid diffusion of O_2 can occur resulting in very rapid oxidation and volatility of the oxide with cracking of the film.

Figure 16 shows a log p_{AlxOy} vs log p_{O_2} diagram for the Al-O system as 1250K. Again a very different diagram is observed. Only one condensed oxide phase is seen in the figure i.e. Al_2O_3. Five vapor species are observed. Al(g) and Al_2O(g) are the important vapor species at the Al-Al_2O_3 interface. Log $p_{Al} = -6.8$ and log $p_{Al_2O} = -8$. These pressures are above the critical value of log $p = -9$ so volatile species can play an important role in the oxidation of intermetallic alloys of important Al activities. Rapid short circuit diffusion of Al through the oxide may occur. In addition the vapor species can diffuse at the Al-Al_2O_3 interface and react with oxygen sealing cracks and defects in the oxide layer to form a protective oxide layer.

Figure 17 shows a log p_{TaxOy} vs log p_{O_2} diagram for the Ta-O system at 1250K. In contrast to the Nb-O system only one oxide is formed Nb_2O_5(s). TaO_2(g) is the main volatile specie at both the Ta(s) - Ta_2O_5(s) and Ta_2O_5 - O_2 interfaces. Very low equilibrium pressures are observed. Volatile species play no role in the oxidation behavior of tantalum. Table 3 summarizes the calculations.

Figure 18 shows a log p_{TixOy} vs log p_{O_2} diagram for the Ti-O system at 1250K. Five oxides phases are observed. Ti(g) is the major volatile specie at the Ti(s) - TiO(s) interface and $TiO_{2(g)}$ is the major volatile specie at the TiO_2(s) - O_2 interface. Very low equilibrium pressures are found. At 1250K volatile metal and oxide species play no role in the oxidation behavior of the titanium. Table 3 summarizes the results.

Figure 19 shows a log p_{CrxOy} vs log p_{O_2} diagram for the Cr-O system at 1250K. Only one oxide is formed, Cr_2O_3(s) Figure 19 shows a new type of diagram. Important pressures of Cr(g) are found at the Cr(s) - Cr_2O_3(s) interface and CrO_3(g) at the Cr_2O_3(s) -O_2 interface. At 1250K volatile species play a role in the oxidation of chromium(32). Volatility is observed for temperatures greater than 1250K and some healing of defects and cracks in the oxide by reaction of Cr(g) with oxygen at defects and cracks. Table 3 summarizes the results.

Conclusions.

Thermochemical analyses of the oxidation of seven metals shows the importance of identifying the condensed phases and the volatile species over the condensed phase.

EXPERIMENTAL STUDY OF THE OXIDATION BEHAVIOR OF SELECTED INTERMETALLIC COMPOUNDS

Introduction

Specimens of various intermetallic compounds were obtained either from arc melted buttons or hot isostatically pressed (HIP) billets. Oxidation coupons 3mm thick were cut from the starting materials, polished through 600 grit SiC, and ultrasonically cleaned. Test coupons were placed in a small quartz crucible suspended by a platinum wire in a thermogravimetric apparatus. Isothermal oxidation of candidate materials was carried out in pure oxygen for times up to 168 hrs. Upon exposure specimens were examined using XRD, SEM, EDS and WDS techniques.

Oxidation of Niobium Trialuminide at 800, 950 and 1100°C

Specimens of $NbAl_3$ were obtained courtesy of Lockheed Palo Alto Laboratories. Hemispherical shaped castings were produced using a micro-arc melting procedure. The aluminum content ranged from 74.2 to 74.4 a/o for these approximately 1/2 inch diameter buttons. The microstructure consisted of irregularly shaped $NbAl_3$ grains delineated by Nb_2Al laden grain boundaries, Figure 20. Nb_2Al and small cracks were visible within individual grains.

Isothermal kinetic data for oxidation runs at 800, 950 and 1100°C are plotted in Figure 21. The two runs at 800°C illustrate the disintegration or "pesting" which occurs at intermediate temperatures. Previous investigators have defined a window of temperature between 550 and 850°C.(1) Note the variation in behavior at 800°C, the first specimen exhibited a 25 hour incubation period while the second degraded rapidly. Both specimens contained 74.4 a/o aluminum. A decrease in the rate of attack was observed as the temperature was raised to 950 and finally 1100°C. The rate of aluminum diffusion should increase with an increase in temperature. Unfortunately, a linear rate was observed at 950 and 1100°C. Svedburg has reported parabolic kinetics and protective alumina scales at 1200°C. (5)

$NbAl_3$, 800°C:

During the incubation period a thin layer of $NbAlO_4$ covers the specimen surface, Figure 22. Preexisting fissures are rapidly filled with a greater volume of this mixed oxide. Preferential attack of grain boundaries and fissures results in fragmentation, Figure 23. An increase in the rate of oxidation occurs as fresh surface area is exposed upon disintegration. The rate levels off as the fragments are surrounded by a layer of $NbAlO_4$.

$NbAl_3$, 1100°C:

At 1100°C the rate of alumina formation appears to be sufficient to compete with that of transient oxidation. A convoluted alumina layer forms between an outer $NbAlO_4$ and an inner Nb_2Al layer, Figure 25. Oxygen again penetrates to form a new alumina layer at the $Nb_2Al/NbAl_3$ interface. The enveloped Nb_2Al is eventually converted to a Nb-Al oxide, repetition of this process results in a layered scale, Figure 26. Note the incipient alumina layers below the Nb_2Al layers in Figure 25 (left) and Figure 26 (right). An interesting feature of the attack is the absence of internal precipitates although no external protective alumina scale was formed. The small difference in stability between alumina and the lowest oxide of Nb (or $NbAlO_4$) may be responsible. Low oxygen solubilities may be important, however, few reliable data have been published.

Oxidation of Nb-Base Alloys containing Al and/or Si at 800 and 1100°C

Arc-melted buttons approximately 2 1/2 inch in diameter were provided courtesy of Pratt and Whitney Aircraft Corporation. A select number of hot isostatically pressed ("hipped") alloys were also provided. Two levels of dissolved oxygen were introduced by varying process parameters. A low level of 500 ppm was introduced using a 2850°F/15 ksi/10 hour treatment. A much higher level was obtained using a 3000°F/20 ksi/5 hour treatment.

The kinetic data at 1100°C are plotted in Figure 27. Although a number of factors are present, it appears that aluminum is more effective than silicon in promoting oxidation resistance. Note the increment between the two upper right hand curves. This improvement was the result of a 12 a/o Si addition at essentially constant Al content. Compare this increment with that immediately below. Here the improvement in performance is due to a 2.5 a/o Al addition at essentially constant Si content. Additions of Ti and/or Ta are known to produce denser, more adherent scales by forming $Nb_2O_5 \bullet TiO_2$ or Ta_2O_5. No pesting was observed, alloys oxidized in essentially the same order at 800°C with rates reduced by a factor of 4.

Nb-Base Alloys, 1100°C:

The morphologies exhibited following oxidation were variants of those shown in Figure 28. Scales consisted of intimate mixtures of oxides of the alloying elements. Levels of Al and Si were too low to support formation of continuous layers. In situ oxidation occurred rapidly, no segregation was indicated by the elemental maps of Figure 28. Backscattered electron images did reveal regions slightly rich in Ta for the alloy containing Ta. Oxygen saturation occurred beneath a growing scale, oxides of Ti were observed within this zone and in advance of it.

Nb-Base Alloys, 800°C:

The morphologies exhibited at 800°C were similar to those exhibited at 1100°C. Scales did contain a greater proportion of the low temperature form of niobium pentoxide. This could be observed optically, scales were often gray or black in constrast to the cream colored scales formed at 1100°C. An enrichment in Ti was observed at the scale/gas interface.

Effects of Initial Structure and Chemistry:

There did not appear to be an advantage in reducing the dissolved oxygen content to 500 ppm. At 1100°C the kinetics were virtually identical, Figure 27. The hipped alloys did not outperform cast alloys to a significant extent. Although the hipped alloys contained fewer defects, the segregation patterns were similar, Figure 29. A major phase rich in Nb, Ti, Al and poor in Si formed in a matrix rich in Nb, Ti, Si and poor in Al for this alloy. Formation of Nb_5Si_3 and/or Nb_3Al was possible depending on the particular case. In any event, in situ oxidation was again so rapid that the major and minor phases oxidized separately.

Oxidation of Tantalum and Molybdenum Disilicide

An important factor in the oxidation of these silicides is the volatility of the base metal oxides. Volatile species diagrams for the Nb, Mo, Si, and Ta-O systems at 1250 K are found in Figures 13 - 15 and 17. It appears that MoO_2(s) should volatilize to MoO_3(v) at these temperatures. The oxides of Nb, Mo and Si appear to not be susceptible to evaporation for short time exposures in pure oxygen.

$TaSi_2$, 800 and 1100°C:

The microstructure of cast $TaSi_2$ is presented in Figure 30. Irregular shaped grains are delineated by free silicon at grain boundaries. This agrees with the binary phase diagram, a $TaSi_2$ + Si field lies adjacent to the line compound. The kinetics for oxidation of $TaSi_2$ and a Ta-67Si-10Al a/o alloy are plotted in Figure 31. At 800°C $TaSi_2$ oxidized with a constantly increasing rate. Thick plates of Ta_2O_5 formed incorporating silicon in discrete regions, Figure 32. Some fragmentation of the specimen was evident. At 1100°C $TaSi_2$ oxidized at a slower rate, but selective oxidation of Si could not support a continuous silica layer, Figure 33. A semi-continuous SiO_2 layer was found in some regions, but other regions were covered by mounds of mixed Ta-Si oxide.

The addition of 10 a/o Al resulted in a lower rate of oxidation at 800°C. Figure 31. Aluminum may have acted as an oxygen getter or formed a barrier upon selective oxidation. The latter has been suggested by preliminary SEM examination. At 1100°C the addition of 10 a/o Al increased the rate of oxidation after an initial transient. The entire alloy was converted to an intimate mixture of Ta, Si and Al oxides. Oxidation of Al to Al_2O_3 may have resulted in catastrophic attack of a Si poor Ta base alloy. If Ta_5Si_3 formed it would have oxidized at a much faster rate than the disilicide. (33)

<u>$MoSi_2$, 600 - 1100°C:</u>

Samples of $MoSi_2$ modified with an Al-Th-Si addition during processing were obtained courtesy of ATS, Inc. The microstructure consisted of Mo_5Si_3 and Al-Th-Si in a matrix of $MoSi_2$, Figure 34. The Al-Th-Si phase is thought to limit pesting by accommodation of stresses. The kinetics at 600, 800 and 1100°C are plotted in figure 35. An interpretation is possible in terms of an interplay between the volatilization of solid transient oxides vs silica formation. (9,34) At 600°C, solid MoO_2 transient oxides disrupt the growth of the silica layer, Figure 36 (top). At 800°C, the volatilization of $MoO_2(s)$ to $MoO_3(v)$ results in a continuous SiO_2 scale, Figure 36 (center). At 1100°C, a semi-continuous SiO_2 layer forms as oxides rich in Th are found at the scale/gas interface, Figure 36 (bottom).

SUMMARY

The above results indicate the complex nature of the oxidation behavior of Nb, Ta, and Mo base intermetallics formed with Al on Si. None of the compounds, with the exception of $MoSi_2$, were capable of forming and maintaining a protective alumina or silica scale over a broad range of temperatures. The mechanisms are seen to involve a combination of rapid transient oxidation which prevents a continuous protective layer from forming. The oxidation mechanisms are being investigated further. Acoustic emission experiments are being conducted to evaluate oxide cracking and low temperature disintegration. Experiments in which an applied electric field will be used in an attempt to modify transient oxidation behavior and the growth of protective scales are planned. Finally, the study is being expanded to include the compound TiAl which has been shown to be an "alumina-former" over certain ranges of conditions (7,22). It is believed that the combination of these experiments with thermochemical analysis will lead to a broad understanding of the mechanisms of oxidation of intermetallic compounds.

REFERENCES

1. E.A. Aitken, "Corrosion Behavior", in Intermetallic Compounds, J.H. Westbrook ed., Wiley, 1967, Chap. 25.

2. R.A. Perkins, Private Communication.

3. C. Wagner, Z. Elektrochem., 63, 772(1959).

4. F. Gesmundo and F. Viani, Oxid. Metals, 25, 269(1986).

5. R. Svedberg, "Oxides Associated with the Improved Air Oxidation Performance of Some Niobium Intermetallics and Alloys" in Properties of High Temperature Alloys, Z.A. Foroulis and F.S. Pettit eds., The Electrochemical Society, 1976, p.331.

6. F.S. Pettit, Trans. TMS-AIME, 239, 1296(1967).

7. G.H. Meier, D. Appalonia, R.A. Perkins, and K.T. Chiang, "Oxidation of Ti-base Alloys" to appear in the Proceedings of the Workshop on the Oxidation of High-Temperature Intermetallics, TMS-AIME, 1989.

8. E. Fitzer, Plansee Proc., 2nd Seminar, Reutte/Tyrol, 1955, Pergamon Press, London, 1956, p.56.

9. J. Berkowitz-Mattuck, P.E. Blackburn, and E.J. Felten, Trans. TMS-AIME, 233, 1093(1965).
J. Berkowitz-Mattuck, M. Rossetti, and D.W. Lee, Met. Trans., 1, 479(1970).

10. J.H. Wood and E. Goldman, "Protective Coatings", in Superalloys II, C.T. Sims, N.S. Stoloff, and W.C. Hagel eds., Wiley, 1987, p. 359.

11. T. Adachi and G.H. Meier, Oxid. Metals, 27, 347(1987).

12. B.M. Warnes, F.S. Pettit, and G.H. Meier, in preparation for Oxid. Metals.

13. C.S. Giggins and F.S. Pettit, J. Electrochem. Soc., 118, 1782(1971).

14. G.R. Wallwork and A.Z. Hed, Oxid. Metals, 3, 171(1971).

15. C.A. Barrett and C.E. Lowell, Oxid. Metals, 11, 199(1977).

16. F.S. Pettit and G.H. Meier, in preparation for Oxid. Metals.

17. R.A. Perkins, K.T. Chiang, and G.H. Meier, Scripta Met., 21, 1505(1987).

18. C.S. Wukusick, "Oxidation Behavior of Intermetallic Compounds in the Nb-Ti-Al System", Report on USAEC Contract No. AT(40-1)-2847, General Electric Corp., July 31, 1963.

19. R.A. Perkins, K.T. Chiang, and G.H. Meier, Scripta Met., 22, 419(1988).

20. R.A. Perkins and C.M Packer, Private Communication.

21. C. Wagner, Corr. Sci., 5, 751(1965).

22. N.S. Choudhury, H.C. Graham, and J.W. Hinze, "Oxidation Behavior of Titanium Aluminides", in Properties of High Temperature Alloys, p. 668.

23. K. Natesan, "Kinetics of Oxidation of Ni Aluminide Exposed to Oxygen-Sulfur Atmospheres", in High Temperature Ordered Intermetallic Alloys II, N.S. Stoloff, C.C. Koch, C.T. Liu, and O. Izumi eds., Materials Research Society, 1987, p. 459.

24. K. Natesan, "Oxidation-Sulfidation of Ni Aluminide in Oxygen-Sulfur Mixed-Gas Atmospheres" in High Temperature Materials Chemistry IV, Z.A. Munir, D. Cubicciotti, and H. Tagawa eds., The Electrochemical Society, 1988, p.89.

25. G.M. Kim and G.H. Meier, "Breakdown of Preformed Oxides on Ni- and Fe-base Alloys in High Sulfur Pressure Atmospheres" in High Temperature Materials Chemistry IV, p. 79.

26. E.A. Gulbransen and G.H. Meier, in 10th Materials Symposium on Characterization fo High Temperature Vapors and Gases, J.W. Hastie ed., N.B.S. Special Publication 561, vol. 2, U.S. Government Printing Office, 1979, p. 1639.

27. E.A. Gulbransen and G.H. Meier, "Thermochemical Stability Diagrams for Condensed Phases and Volatility Diagrams for Volatile Species over Condensed Phases in Twenty Metal-Sulfur-Oxygen Systems between 1150 and 1450K", Report on U.S. Department of Energy Contract DE-AC01-79-ET-13547, Univ. of Pittsburgh, 1980.

28. JANAF Thermochemical Tables, NBS 37, U.S. Government Printing Office, 1971.

29. JANAF Thermochemical Tables, 1975 Supplement, Reprint No. 60 from J. Phys. and Chem. Ref. Data, 4, 1(1975).

30. JANAF Thermochemical Tables, 1978 Supplement, Reprint No. 120 from J. Phys. and Chem. Ref. Data, 7, 793(1978).

31. E.A. Gulbransen, K.F. Andrew, and F.A. Brassart, J. Electrochem. Soc., 110, 242(1963).

32. G.C. Fryburg, F.J. Kohl, and C.A. Stearns, J. Electrochem. Soc., 121, 952(1974).

33. Niobium 1980, AIME, 1980.

34. Binary Alloy Phase Diagrams, T.B. Massalski ed., ASM, 1986.

35. A.G. Metcalfe and A.R. Stetson, "Interactions in Coated Refractory Metal Systems", AIME Metallurgical Society Proceedings on Refractory Metal Alloys, J.Machlin, R.T. Begley, and E.D. Weisert eds., Plenum Press, 1968, p. 129.

36. R.W. Bartlett, J.W. McCamont, and P.R. Gage, J. Amer. Ceram. Soc., 48, 551(1965).

TABLE 1

Physical Properties of the Seven Metals and Their Oxides

See Table 2 for References

Metal	M.P.K.	B.P.K.	Condensed Oxides	M.P.K.	B.P.K.	Volatile Species
Al	933	2767	Al_2O_3	2321		Al,AlO,AlO_3
						Al_2O,Al_2O_2
Cr	2176	2915	Cr_2O_3	2603 ± 15		Cr,CrO,CrO_2,
			Cr_2O_3			CrO_3
			CrO_3			
			CrO_6			
Mo	2892	4919	MoO_2			Mo,MoO,MoO_2
			MoO_3	1074	1428	MoO_3,$(MoO_3)_3$
Nb	2750	3156	NbO	2210		Nb,NbO,NbO_2
			NbO_2	2175		
			Nb_2O_5	1783		
Si	1685	3492	SiO_2	1996		Si,Si_2,Si_3,
						SiO,SiO_2
Ta	3258	5786	Ta_2O_3	2058 ± 30		Ta,TaO,TaO_2
Ti	1933	3591	Sub-oxides			
			Ti_6O,Ti_3O			Ti,TiO,TiO_2
			Ti_2O,Ti_3O_2			
			TiO	2023		
			Ti_2O_3	2115		
			Ti_3O_5	2050		
			Ti_4O_7	1950		
			TiO_2	2130		

Table 2 Thermochemical Data M-O Systems 800-1459k

Compound	Ref.	M.P.K.	Log k_p at T.K. 800	900	1000	1150	1250	1342	1459
					Aluminum				
Al_2O_3(s)	5	2723 ± 6	93.04	80.88	71.09	59.60	53.45	48.59	43.70
Al(g)	2	933	-14.29	-11.95	-10.13	-8.075	-6.905	-6.023	-5.136
AlO(g)	5		-0.075	0.384	0.704	1.042	1.219	1.355	1.439
AlO_2(g)	5		12.83	11.45	10.31	8.932	8.194	7.610	7.019
Al_2O(g)	5		13.41	12.40	11.51	10.39	9.78	9.30	8.80
Al_2O_2(g)	5		28.95	25.74	23.08	19.90	18.19	16.84	15.46
					Chromum				
Cr_2O_3(s)	4	2603 ± 15	60.13	51.96	45.44	37.80	33.72	30.50	2725
CrO_6(l)	7	470		22.7	19.5	15.76	13.75	12.22	10.53
Cr(g)	4		18.18	-15.32	-13.04	-10.38	-8.96	-7.84	-6.72
CrO(g)	4		-6.533	-5.201	-4.142	-2.91	-2.26	-1.75	-1.24
CrO_2(g)	4		6.872	6.292	5.822	5.26	4.96	4.71	4.46
CrO_3(g)	4		15.60	13.46	11.74	9.72	8.64	7.78	6.91

				Molybdenum					
$MoO_2(s)$	3		28.95	24.73	21.36	17.43	15.34	13.70	12.05
$MoO_3(s,l)$	3	1074	35.40	30.06	25.80	20.96	18.54	16.61	14.67
Mo(g)	3		-35.06	-30.30	-26.51	-22.06	-19.69	-17.82	-15.93
MoO(g)	3		-19.84	-17.06	-14.85	-12.26	-10.88	-9.792	-8.699
$MoO_2(g)$	3		3.011	2.887	2.784	2.66	2.59	2.53	2.46
$MoO_3(g)$	3		20.55	17.92	15.82	13.36	12.04	11.00	9.95
$1/3\ (MoO_3)_3\ (g)$	6		33.07	28.49	24.90	20.55	18.29	16.50	14.67
				Niobium					
NbO(s)	4	2210	22.61	19.59	17.17	14.34	12.83	11.64	10.44
$NbO_2(s)$	4	2175	42.60	36.59	32.03	26.71	23.89	21.67	19.43
$Nb_2O_5(s)$	4	1785	101.01	87.34	76.41	63.65	56.83	51.46	46.04
Nb(g)	4	2750	-39.97	-34.65	-30.39	-25.40	-22.75	-20.62	-18.50
NbO(g)	4		-7.912	-6.50	-5.38	-4.07	-3.38	-2.83	-2.28
$NbO_2(g)$	4		14.51	13.03	11.84	10.44	9.69	9.10	8.50
$MoO_3(g)$	3		20.55	17.92	15.82	13.36	12.04	11.00	9.95
$1/3\ (MoO_3)_3\ (g)$	6		33.07	28.49	24.90	20.55	18.29	16.50	14.67

Silicon

SiO_2(s)	3	1996	49.99	43.41	38.15	31.99	28.72	26.12	23.53
Si(g)	3	1683	-21.65	-18.39	-15.79	-12.74	-11.11	-9.83	-8.535
Si_2(g)	3		-28.36	-24.39	-20.99	-17.03	-14.91	-13.24	-11.56
Si_3(g)	3		-30.66	-26.09	-22.44	-18.19	-15.92	-14.13	-12.34
SiO(g)	3		11.15	10.40	9.787	9.067	8.678	8.369	8.054
SiO_2(g)	3		20.13	17.90	16.11	14.02	12.90	12.01	11.16

Tantalum

Ta_2O_5(s)	4	2058 ± 3-	110.63	95.63	83.87	70.12	62.79	57.01	51.18
Ta(g)	4	3258	-43.64	-37.98	-33.45	-28.15	-25.31	-23.07	-20.81
TaO(g)	4		-7.66	-6.302	-5.217	-3.953	-3.280	-2.750	-2.218
TaO_2(g)	4		14.72	13.23	12.04	10.63	9.88	9.280	8.674

Titanium

TiO(s)	4	3023	30.36	26.45	23.32	19.66	17.70	16.16	14.62
Ti_2O_3(s)	4	2115	84.50	73.59	64.87	54.66	49.20	44.91	40.57
Ti_3O_5(s)	4	2050	136.83	119.18	105.08	88.53	79.69	72.70	65.66
Ti_4O_7(s)	4	1950	189.33	164.79	145.18	122.18	109.90	100.22	90.44
TiO_2(s)	4	2130	52.12	45.30	39.84	33.44	30.02	27.33	24.60
Ti(g)	3	1933	-23.13	-19.72	-17.00	-13.83	-12.15	-10.82	-9.49
TiO(g)	4		1.538	1.899	2.182	2.498	2.654	2.771	2.885
TiO_2(g)	4		21.05	18.80	16.99	14.86	13.71	12.79	11.86

Table 3
Summary Thermochemical analyses

Metal	Oxide	Logp_{O_2} (atm)	interface	Vapor Specie	Log p (atm)	Protective Oxide
Al(l)	Al_2O_3(s)	-35.63	Al/Al_2O_3	Al	-6.905	yes
			Al/Al_2O_3	Al_2O	-8.037	
			Al_2O_3/O_2	AlO_2	-18.53	
Cr(s)	Cr_2O_3	-22.45	C Cr_2O_3	Cr	-8.96	yes
			Cr_2O_3/O_2	CrO_3	-8.02	
Mo(s)	MoO_2	-15.34	Mo/MoO_2	MoO_3	-10.97	no
	MoO_3		MoO_3/O_2	$(MoO_3)_3$	-0.74	
Nb(s)	NbO	-25.66	Nb/NbO	NbO_2	-15.97	no
	NbO_2		NbO/NbO_2	NbO_2	-14.20	
	Nb_2O_5		Nb_2O_5/O_2	NbO_2	-22.12	
Si(s)	SiO_2	-28.72	Si/SiO_2	SiO	-5.43	yes
			SiO_2/O_2	SiO	-20.04	
Ta(s)	Ta_2O_5	-25.116	Ta/Ta_2O_5	TaO_2	-15.236	no
			Ta_2O_5/O_2	TaO_2	-21.515	
Ti(s)	TiO	-35.40	Ti/TiO	Ti	-12.15	no
	Ti_2O_3		Ti_4O_7/TiO_2	TiO_2	-16.31	
	Ti_3O_7		TiO_2/O_2	TiO_2	-16.31	
	Ti_4O_7					
	TiO_2					

FIGURES

Figure 1. Melting points and densities of selected intermetallics

Figure 2. Standard free energies of formation for selected oxides.

Figure 3. Schematic diagram of the oxidation of a noble metal, A, containing a reactive metal, B. a) Dilute alloy showing internal oxidation of B. b) Concentrated alloy forming an external layer of BO.

Figure 4. Schematic of oxidation of A-B with both AO and BO stable (BO more stable than AO). a) Dilute alloy showing internal oxidation under external AO. b) Concentrated alloy forming external BO.

Figure 5. Schematic cross-section of $MoSi_2$ forming a silica scale.

Figure 6. Map of the selective oxidation behavior of Ni-Al alloys as a function of temperature and Al-content (ref. 6).

Figure 7. The binary phase diagram for the Ti-Al system showing the region in the TiAl field where alumina scales form in pure oxygen.

Figure 8. Schematic plot comparing isothermal and cyclic oxidation rates.

Figure 9 . Weight change vs time data for cyclic oxidation of several Ni-silicides in air (Compositions in wt. pct).

Figure 10. Isothermal (a) and cyclic (b) oxidation maps for the Ni-Cr-Al system showing the effect of Cr in developing and maintaining a protective alumina scale.

Figure 11. Map of oxygen pressure vs. temperature indicating conditions for the development of a protective silica film on $MoSi_2$ and the importance of volatile species in this process.

Figure 12 Bar chart summarizing the oxidation behavior of the most resistant compound in each of the indicated systems. The maximum temperature generally corresponds to 20 mg/cm^2 in 100 hours.

Figure 29. Comparison of starting materials and structures following 168 hrs. oxidation at 1100°C for a Nb-Ti-Al-Si alloy which was prepared by casting and by hipping.

Figure 30. Initial microstructure of $TaSi_2$ (dark phase is elemental Si).

Figure 31. Weight change vs. time data for $TaSi_2$ and Al-modified $TaSi_2$ oxidized in oxygen at 800 and 1100°C.

Figure 32. Surface (top) and cross-section (bottom) of $TaSi_2$ after 168 hrs oxidation at 800°C. The lighter phase is Ta_2O_5 and the dark phase is SiO_2.

Figure 33. Cross-sections of $TaSi_2$ oxidized 168 hrs. at 1100°C showing exclusive formation of a silica film over some areas (top) and Ta-rich nodules over others (bottom).

Figure 34. Initial microstructure of "$MoSi_2$". (White phase is Mo_5Si_3 and the dark phase is SiO_2). Th was detected adjacent to the silica regions.

Figure 35. Weight change vs. time data for $MoSi_2$ oxidized in oxygen at 600, 800, and 1100°C.

Figure 36. Top: Surface of $MoSi_2$ after 168 hrs. oxidation at 600°C.
Center: Surface(left) and cross-section(right) of $MoSi_2$ after 168 hrs. oxidation at 800°C.
Bottom: Surface of $MoSi_2$ after 168 hrs. oxidation at 1100°C.

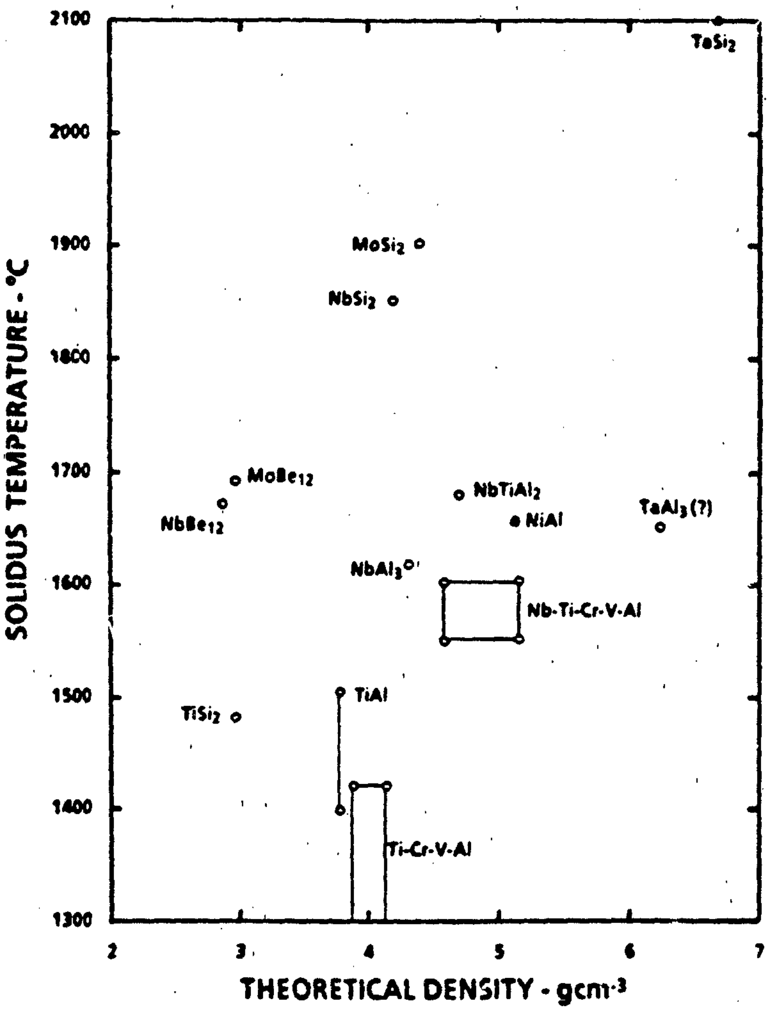

Figure 1. Melting points and densities of selected intermetallics.

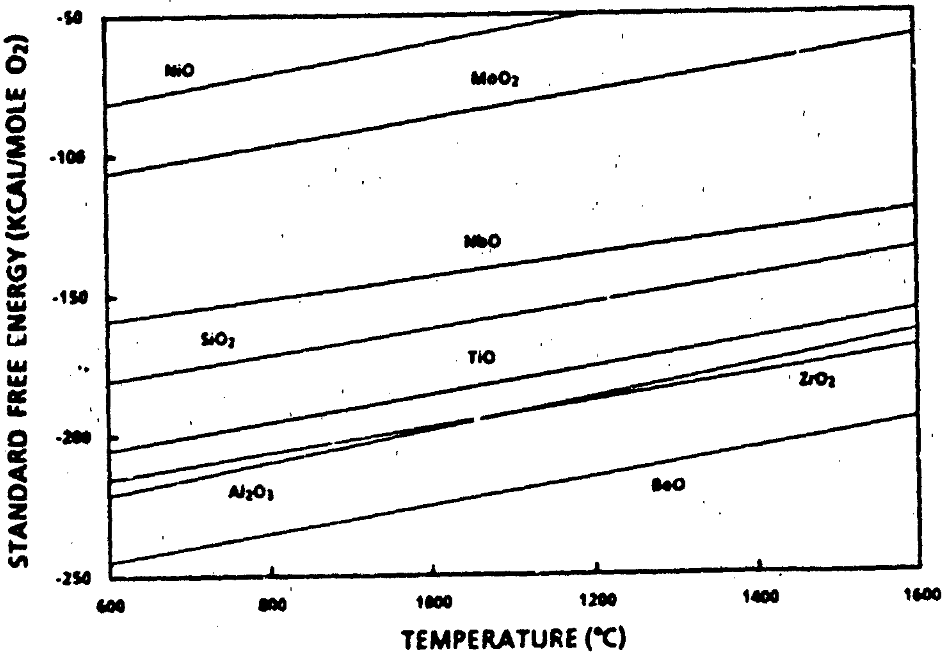

Figure 2. Standard free energies of rormation for selected oxides.

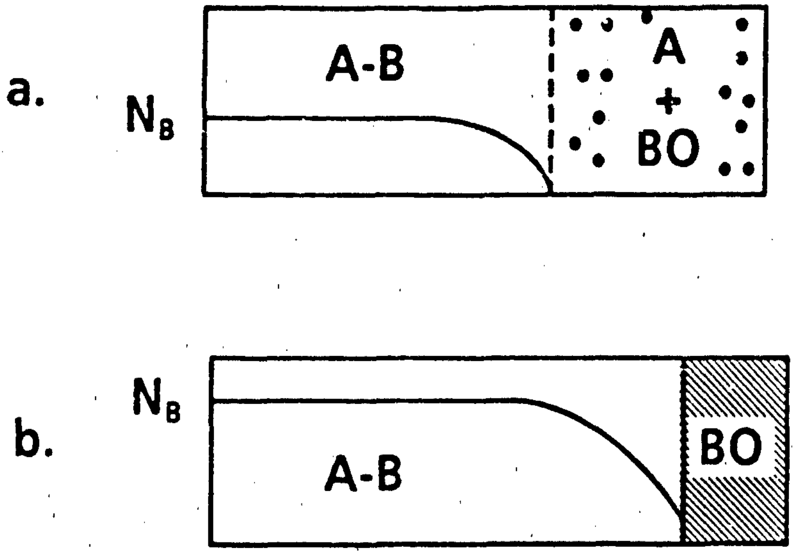

Figure 3. Schematic diagram of the oxidation of a noble metal, A, containing a reactive metal, B. a) Dilute alloy showing internal oxidation of B. b) Concentrated alloy forming an external layer of BO.

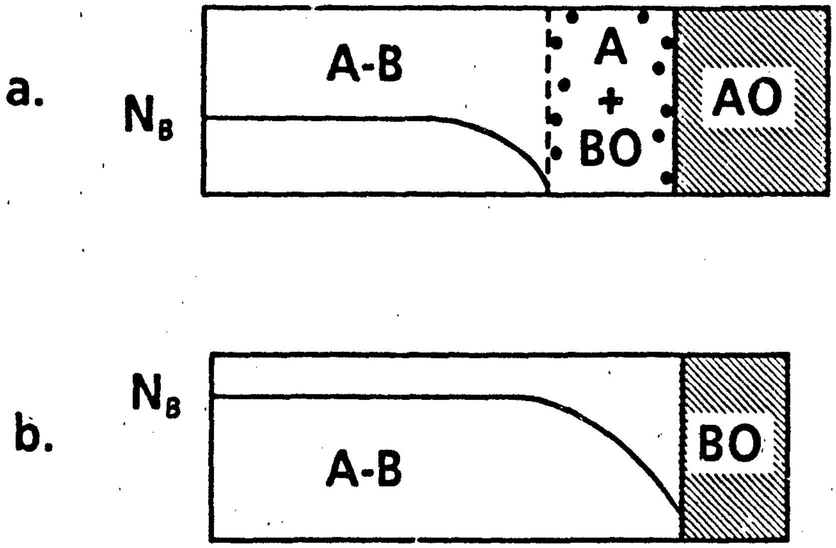

Figure 4. Schematic of oxidation of A-B with both AO and BO stable (BO more stable than AO). a) Dilute alloy showing internal oxidation under external AO. b) Concentrated alloy forming external BO.

$$MoSi_2 + \frac{7}{5}O_2 = \frac{1}{5}Mo_5Si_3 + \frac{7}{5}SiO_2$$

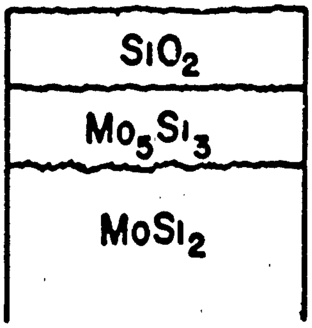

Figure 5. Schematic cross-section of $MoSi_2$ forming a silica scale.

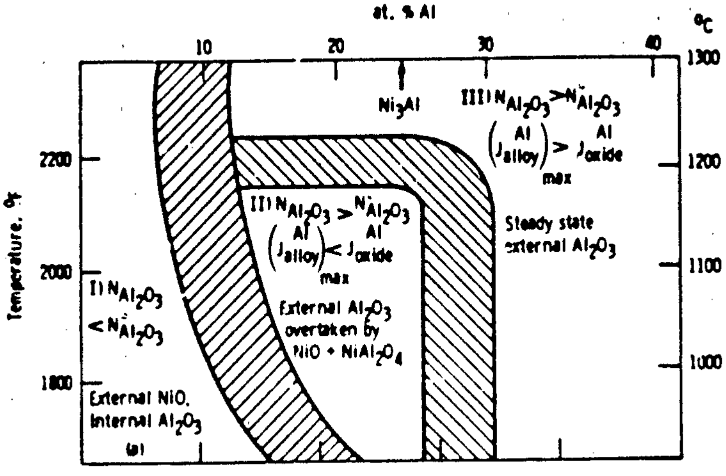

Figure 6. Map of the selective oxidation behavior of Ni-Al alloys as a function of temperature and Al-content (ref. 6).

Figure 7. The binary phase diagram for the Ti-Al system showing the region in the TiAl field where alumina scales form in pure oxygen.

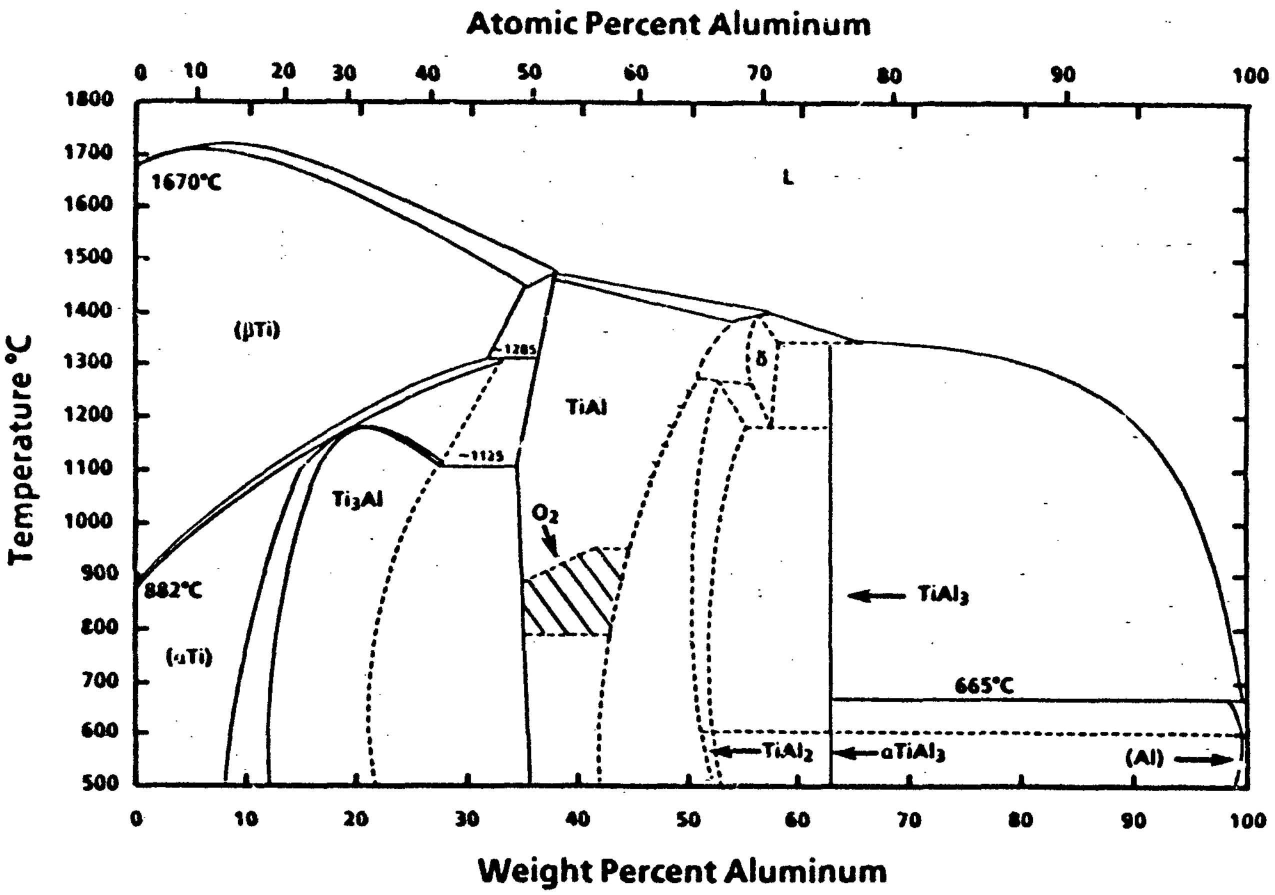

Figure 8. Schematic plot comparing isothermal and cyclic oxidation rates.

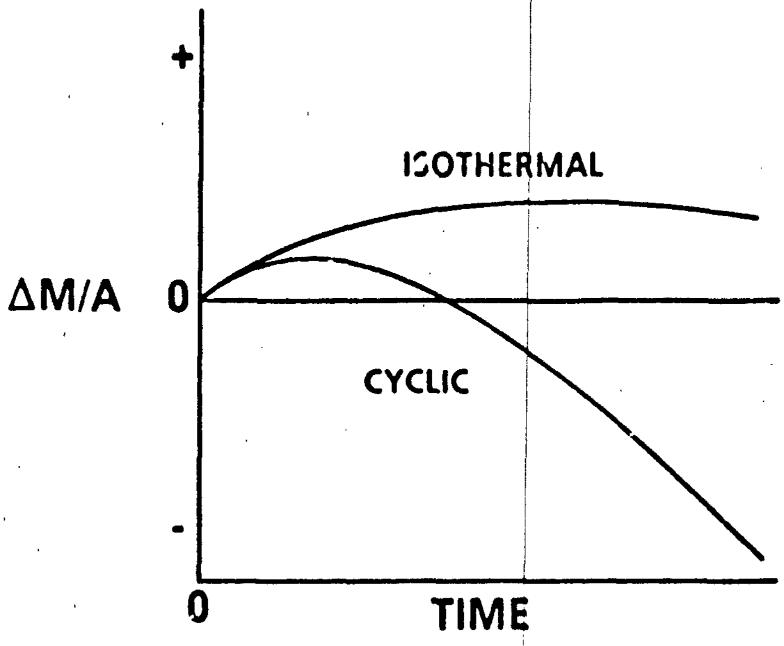

Figure 9 . Weight change vs time data for cyclic oxidation of several Ni-silicides in air (Compositions in wt. pct).

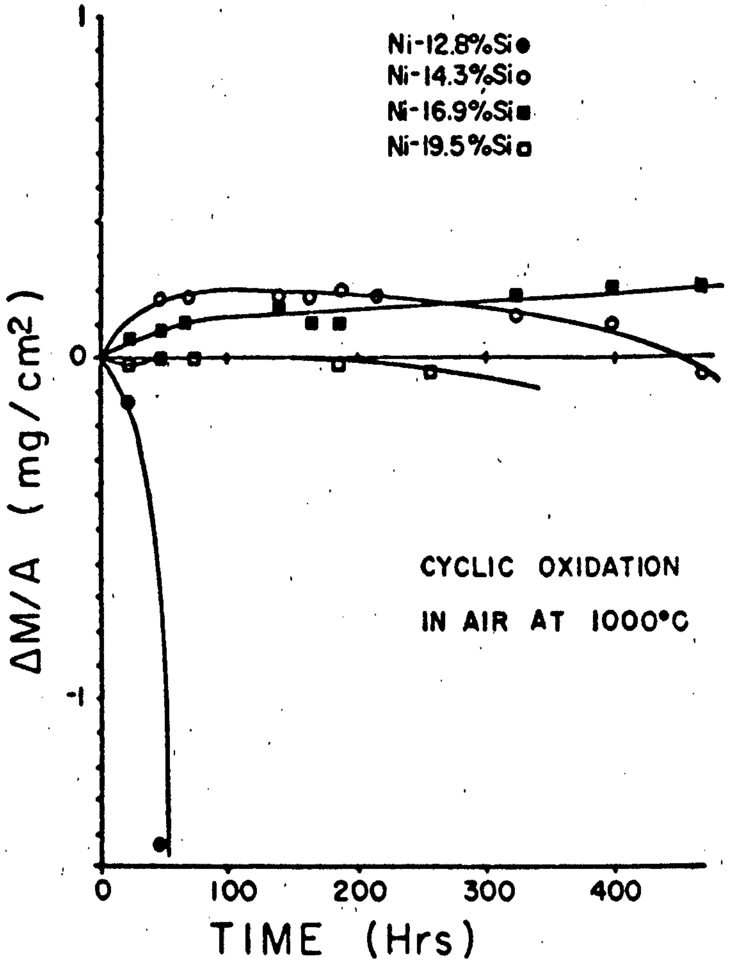

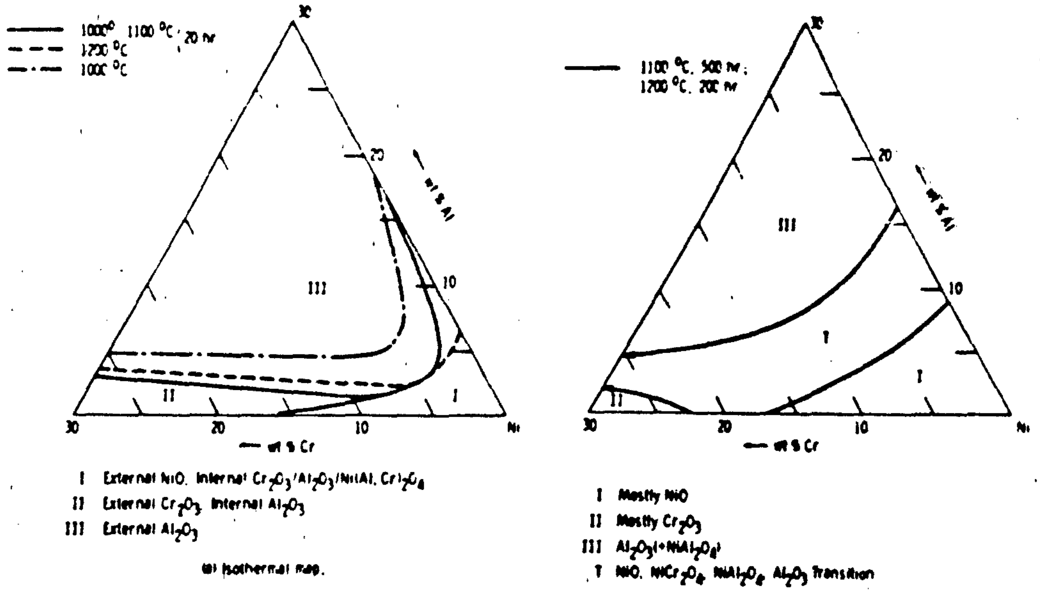

(a) Isothermal map.

(b) Cyclic map.

Figure 10. Isothermal (a) and cyclic (b) oxidation maps for the Ni-Cr-Al system showing the effect of Cr in developing and maintaining a protective alumina scale.

Figure 11. Map of oxygen pressure vs. temperature indicating conditions for the development of a protective silica film on $MoSi_2$ and the importance of volatile species in this process.

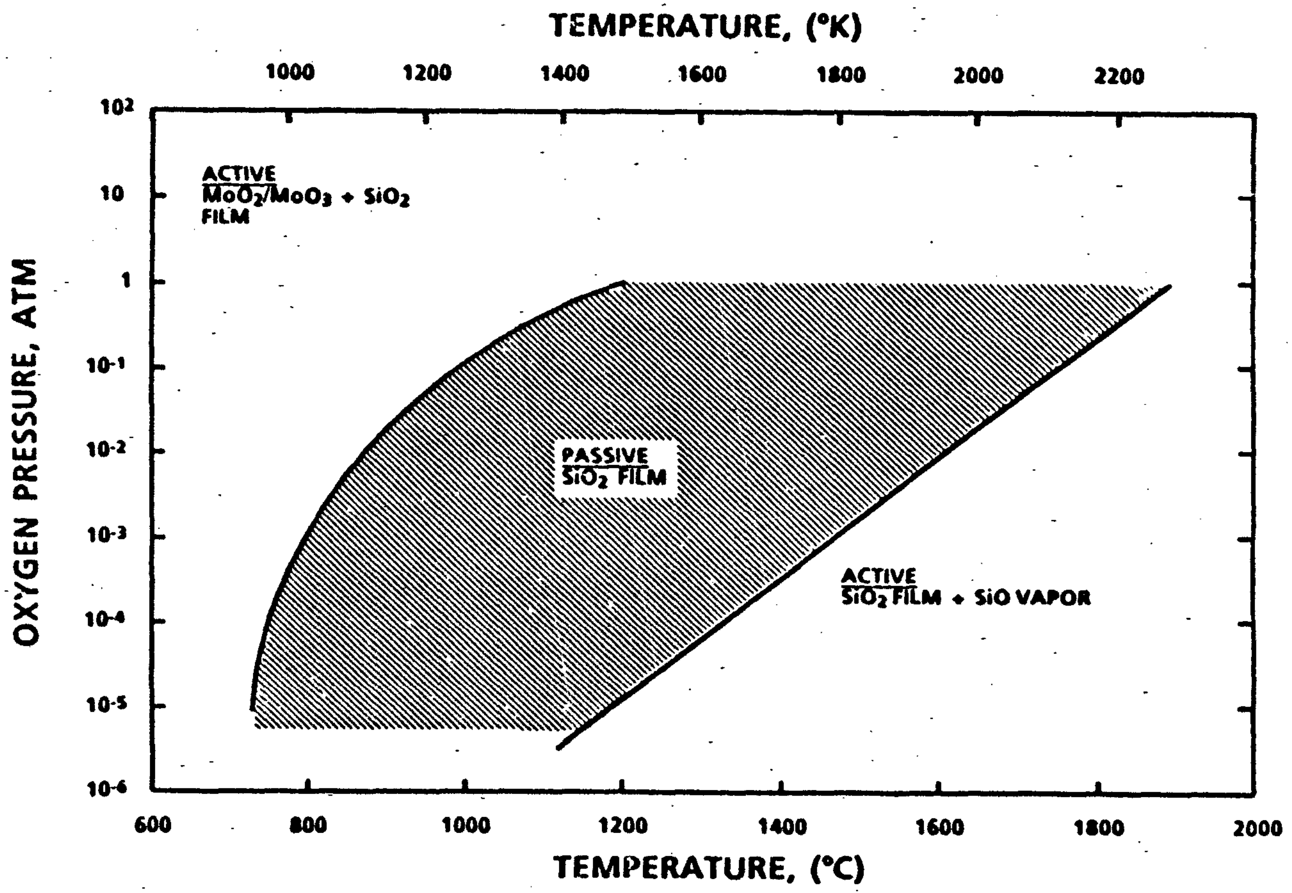

Figure 12. Bar chart summarizing the oxidation behavior of the most resistant compound in each of the indicated systems. The maximum temperature generally corresponds to 20 mg/cm^2 in 100 hours.

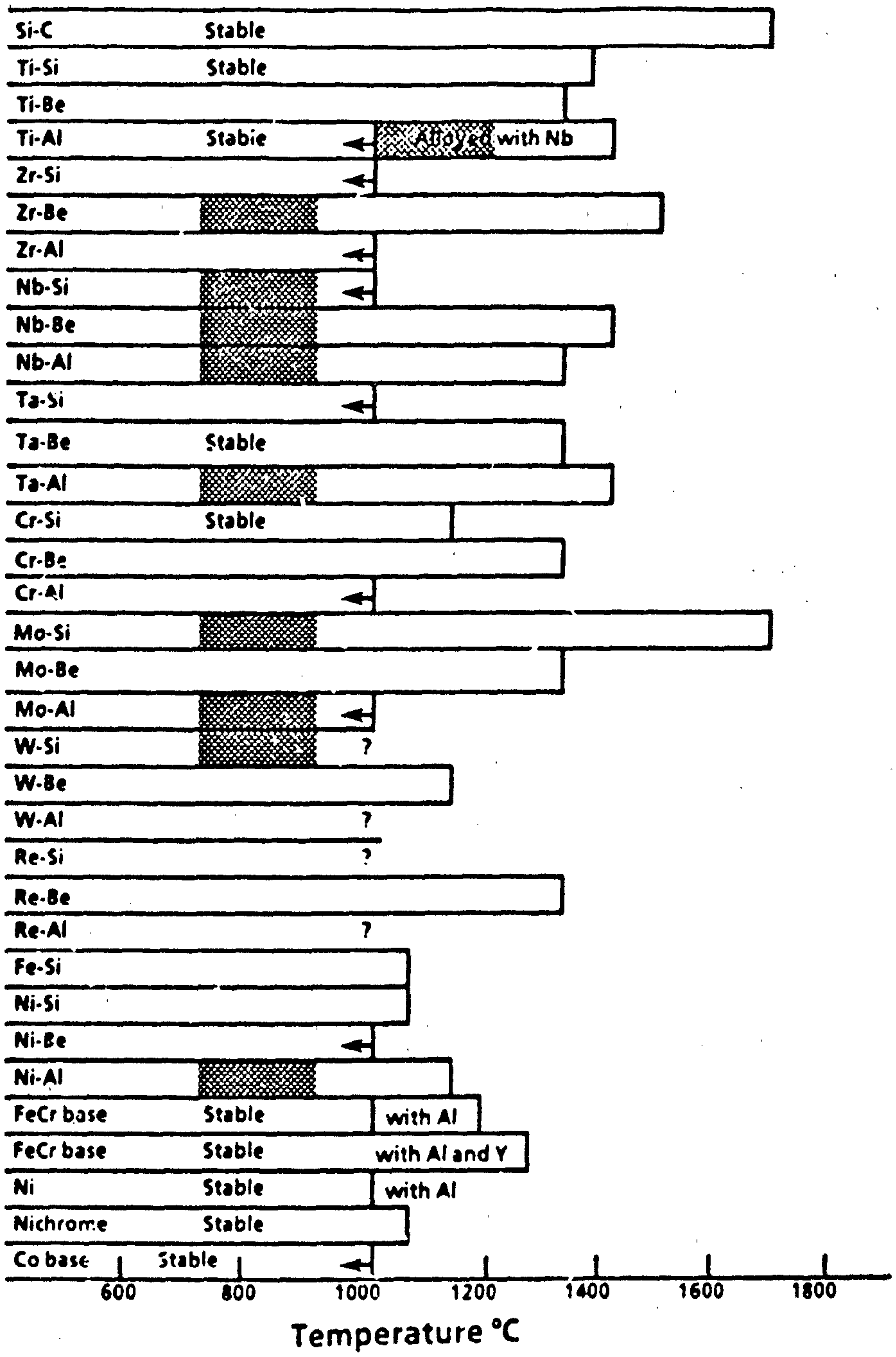

Figure 13. Volatile species for the Nb-O system at 1250K.

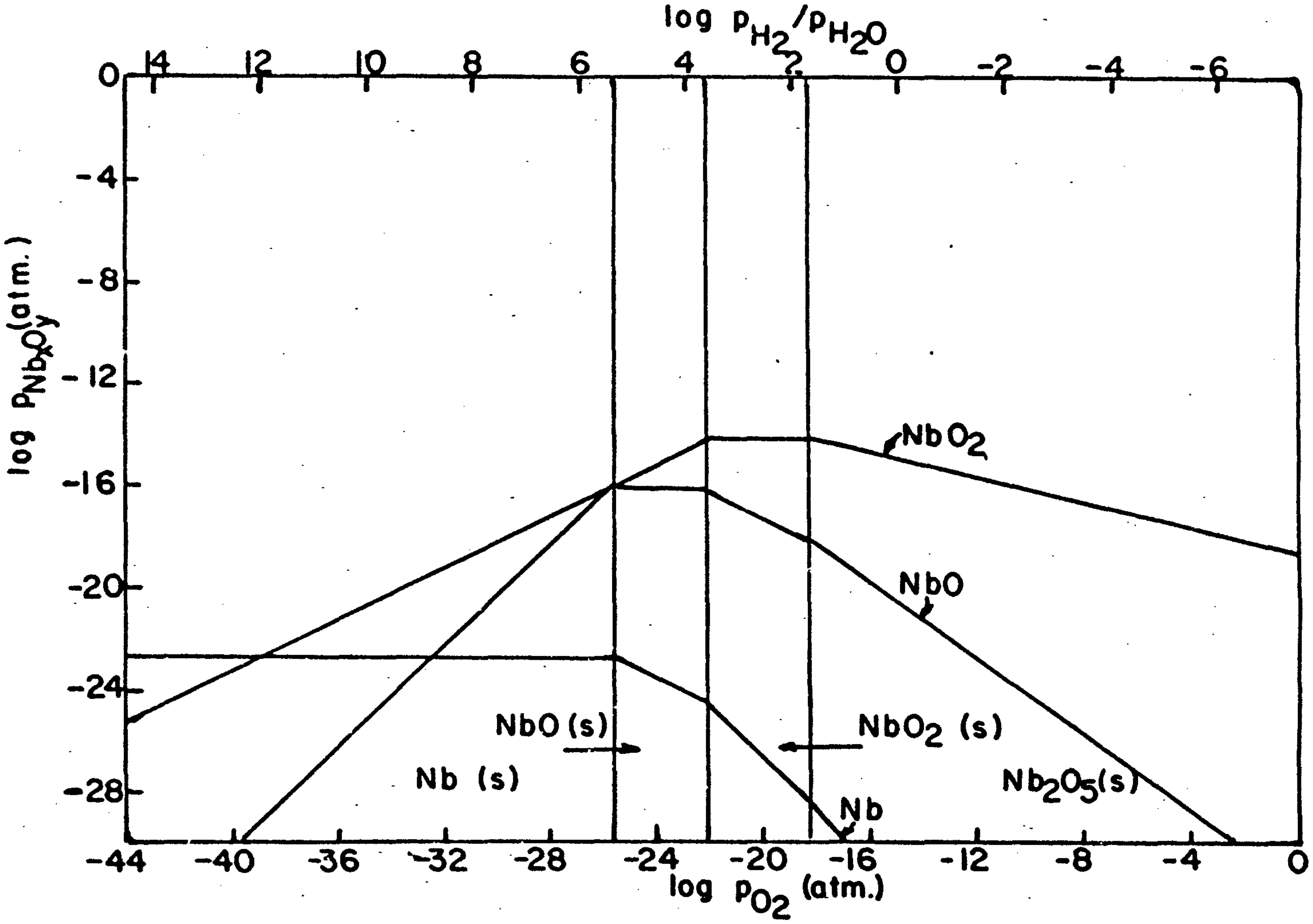

Figure 14. Volatile species for the Mo-O system at 1250K.

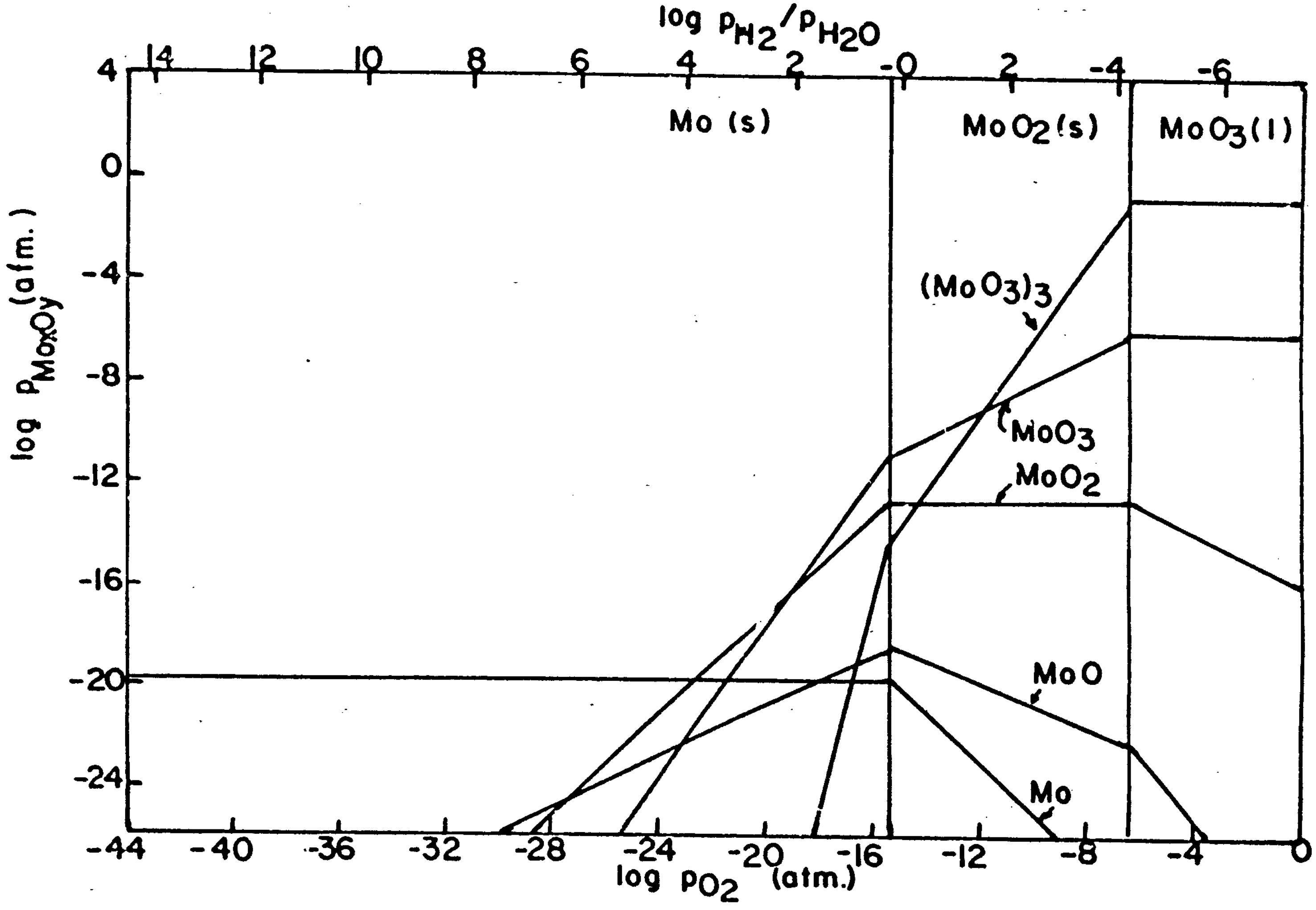

Figure 15. Volatile species for the Si-O system at 1250K.

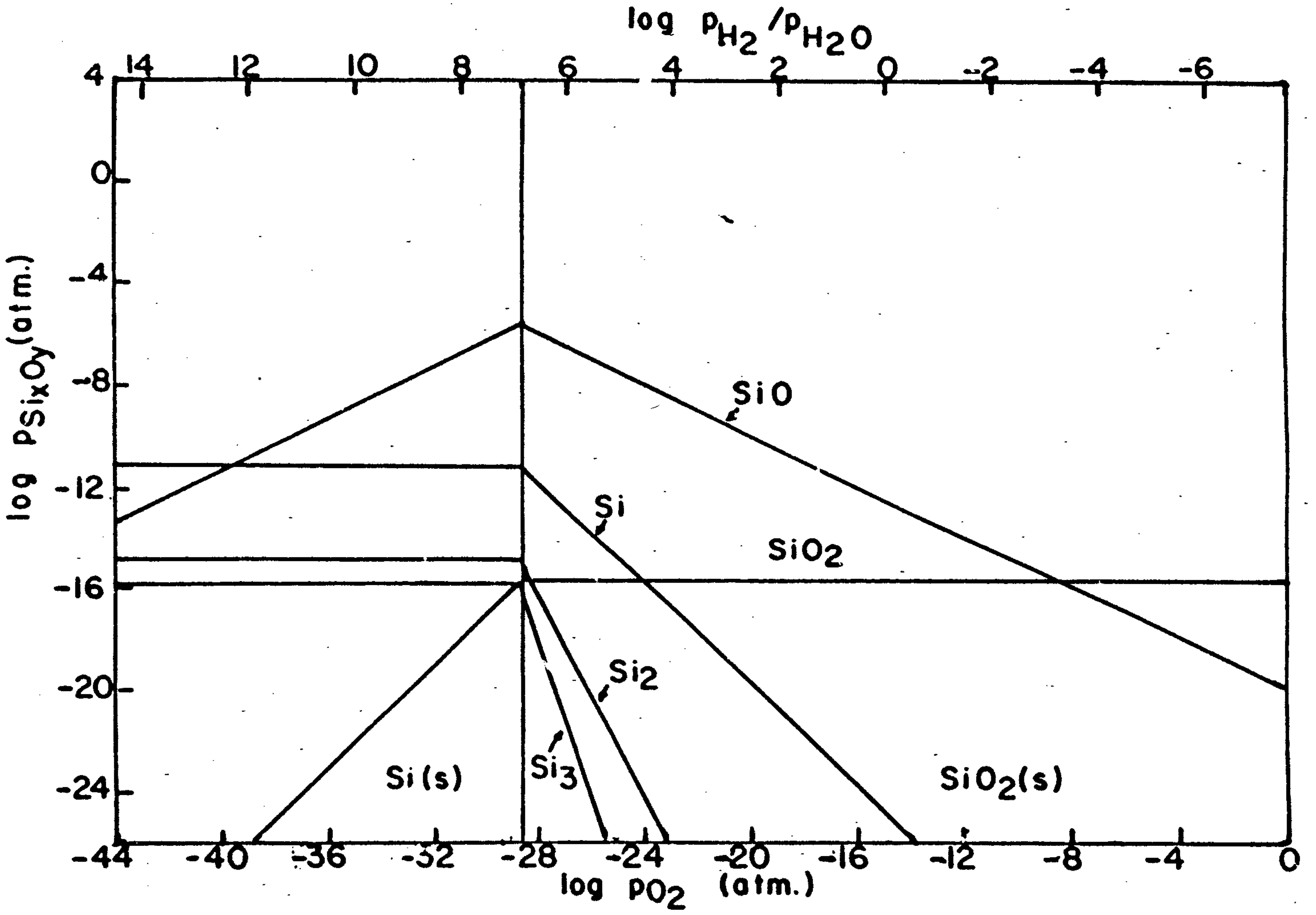

Figure 16. Volatile species for the Al-O system at 1250K.

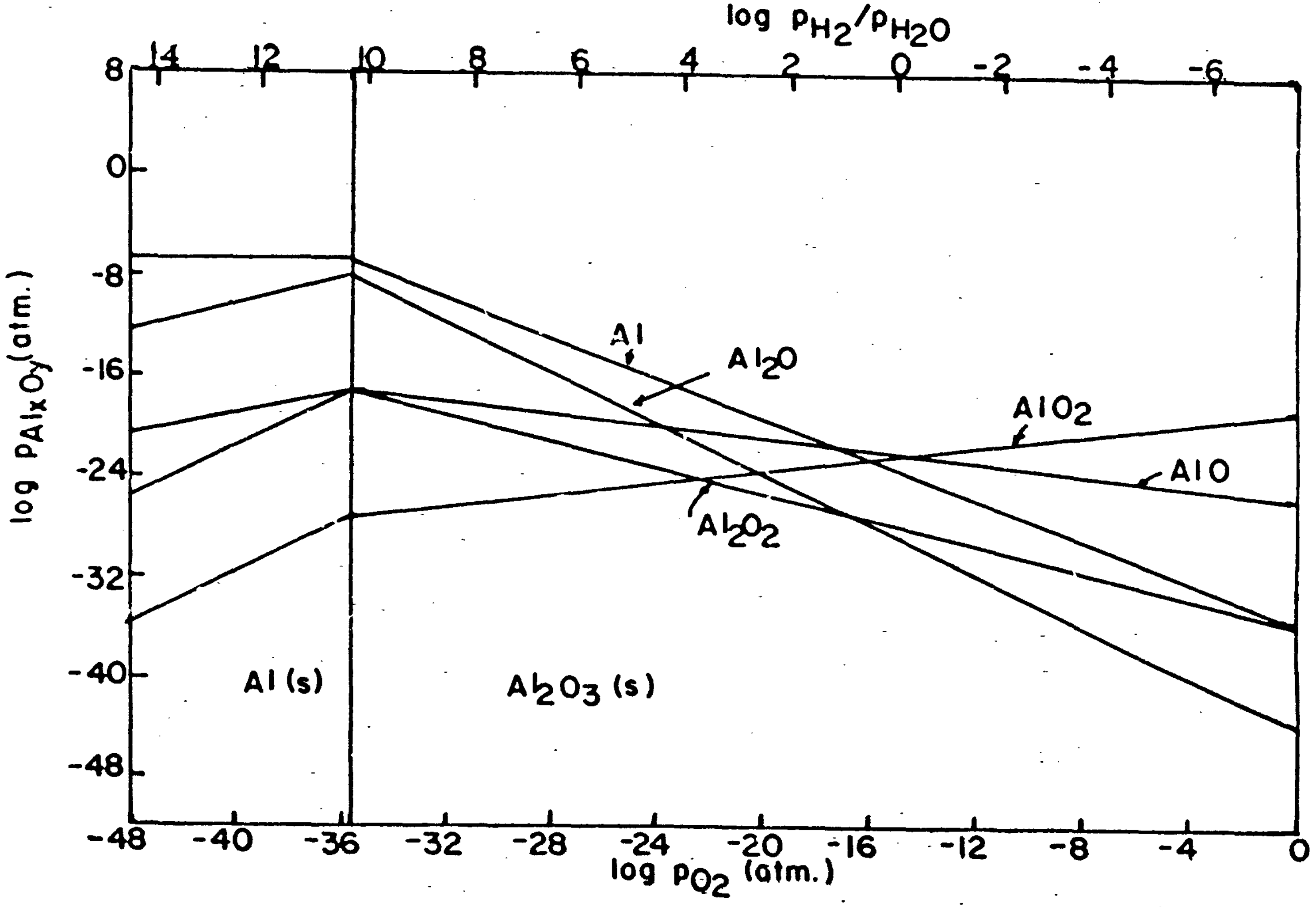

Figure 17. Volatile species for the Ta-O system at 1250K.

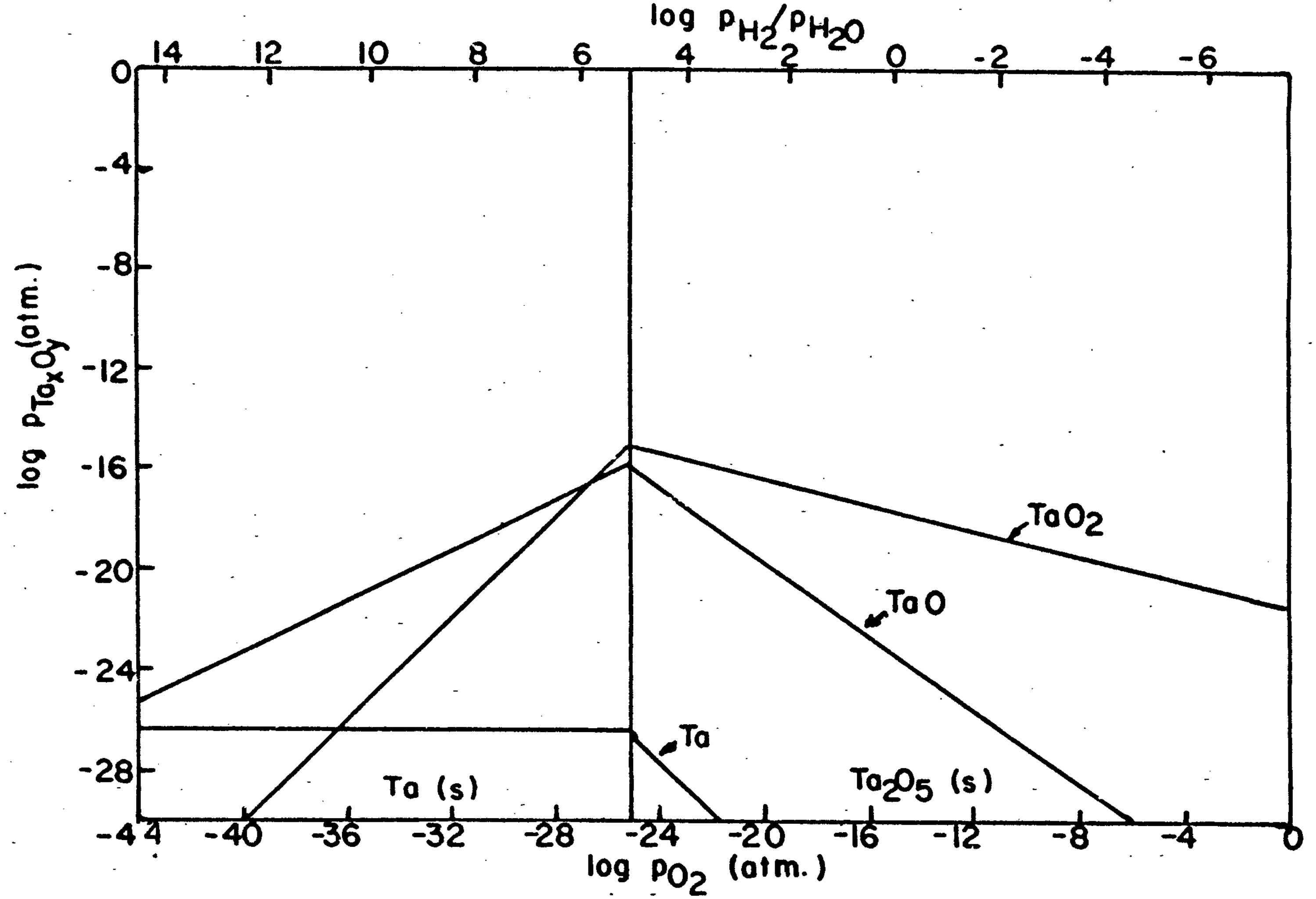

Figure 18. Volatile species for the Ti-O system at 1250K.

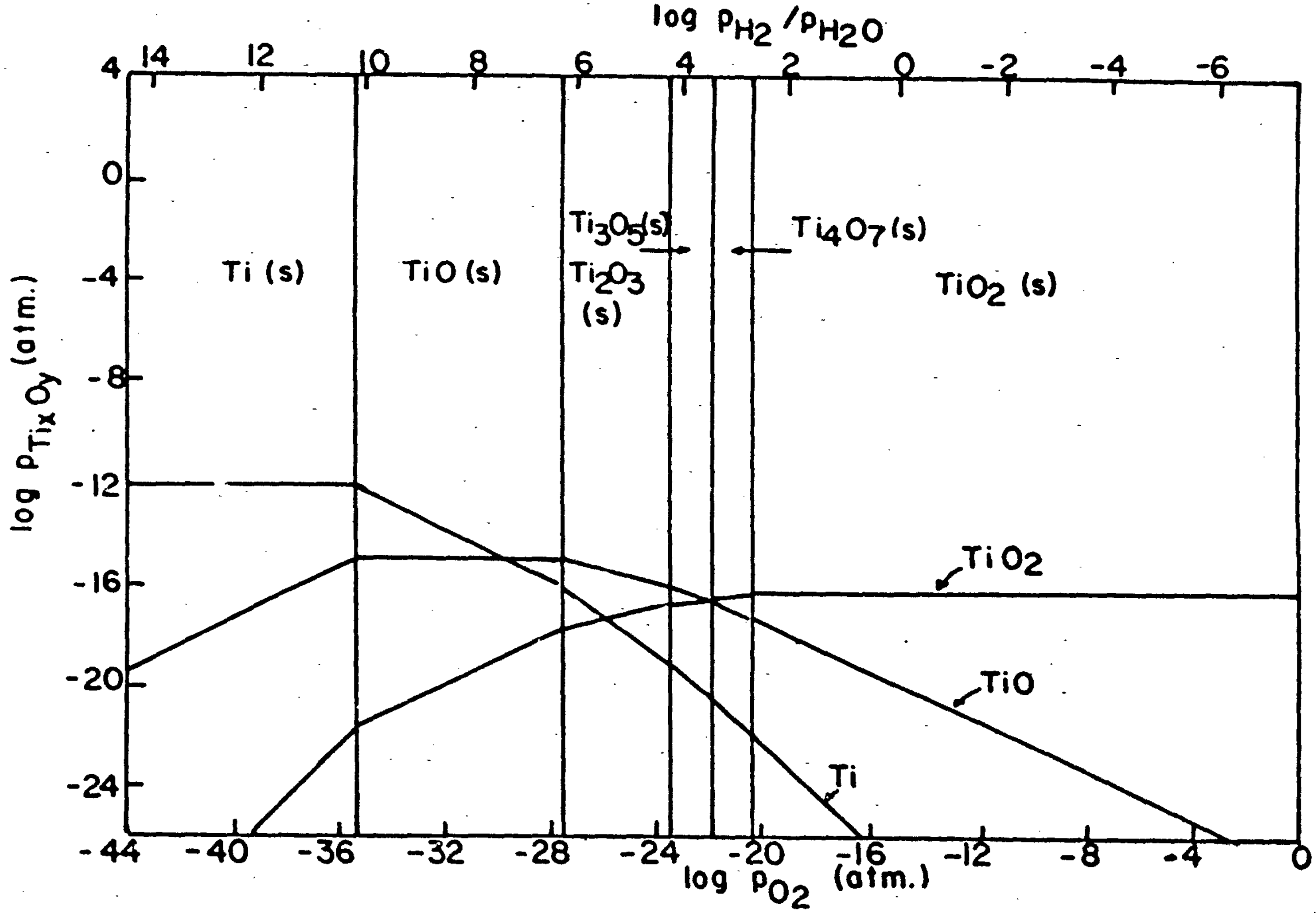

Figure 19. Volatile species for the Cr-O system at 1250K.

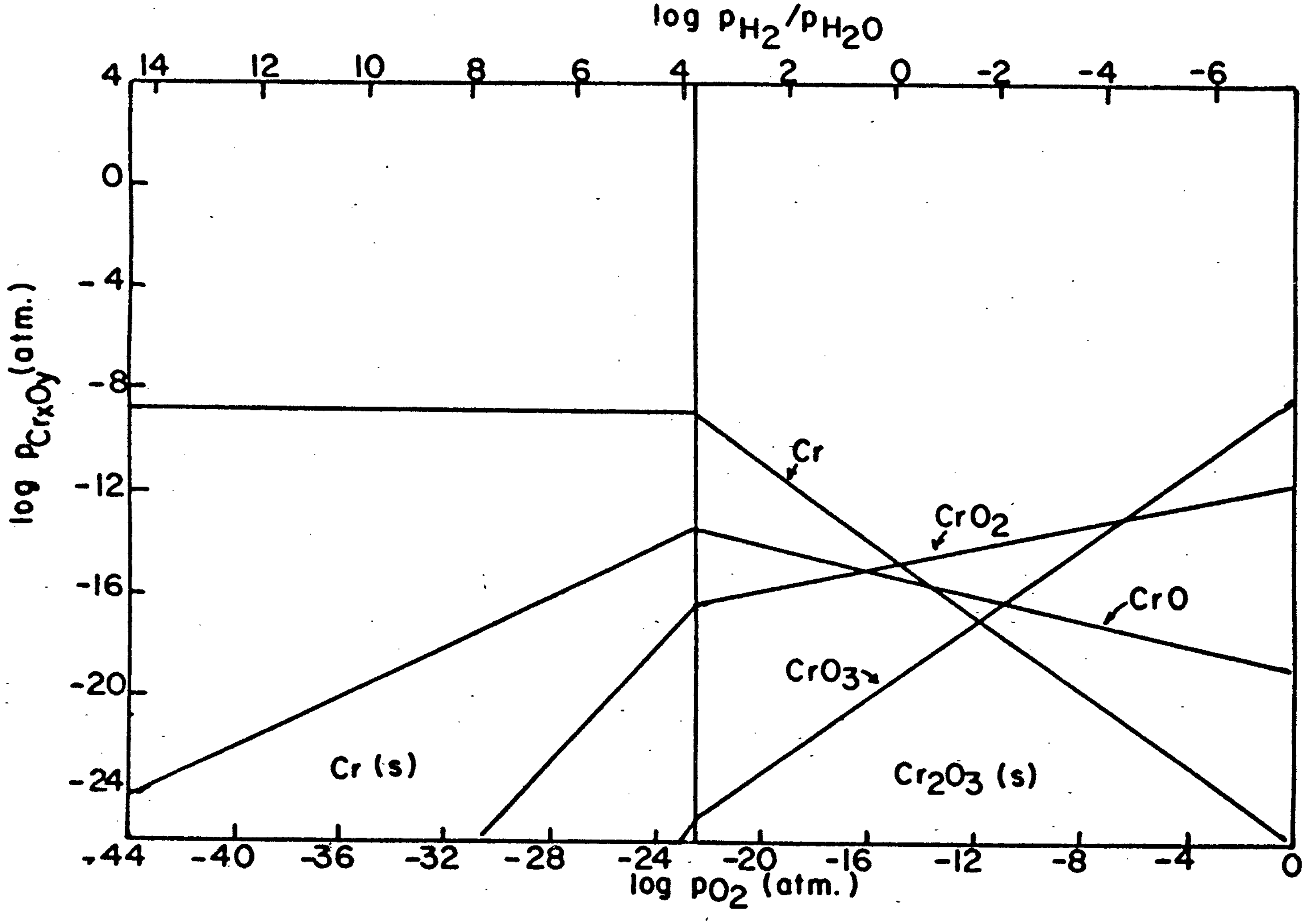

Microstructure of Niobium Aluminide

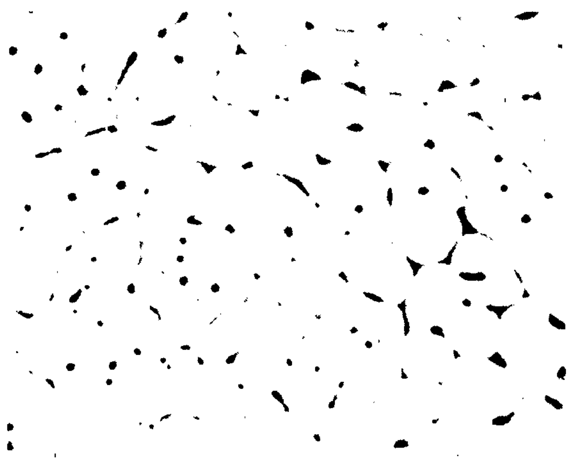

Figure 20. Initial microstructure of $NbAl_3$ (Dark phase is Nb_2Al).

Figure 21. Weight change vs. time data for $NbAl_3$ oxidized in oxygen at 800, 950, and 1100°C.

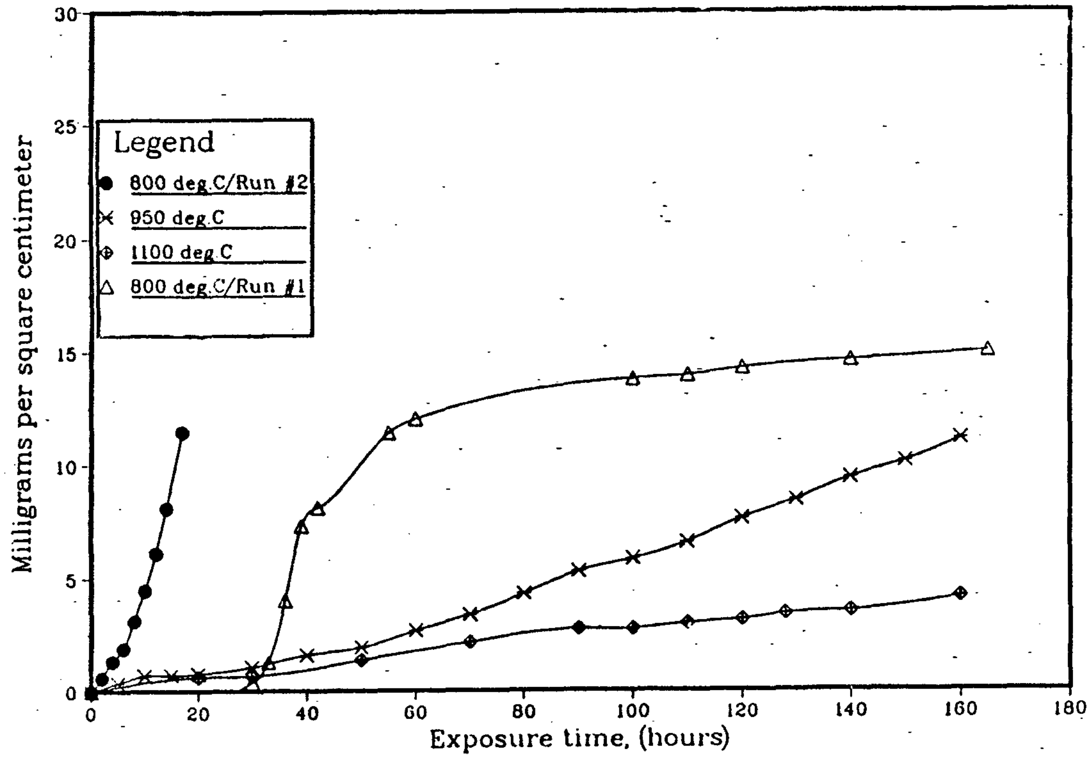

Niobium Aluminide

800°C-5 Hours

Figure 22. Surface of $NbAl_3$ after 5 hrs. oxidation in oxygen at 800°C showing a thin layer of $NbAlO_4$ and a pre-existing crack.

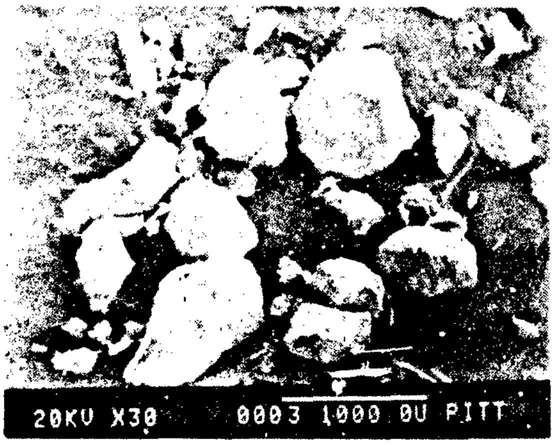

$NbAl_3$ 24hr Oxygen 800 C
Shows Result of "Pesting"

Figure 23. Micrograph of $NbAl_3$ showing "pesting" after 24 hrs. oxidation in oxygen at 800°C.

[illegible] Oxygen 950C

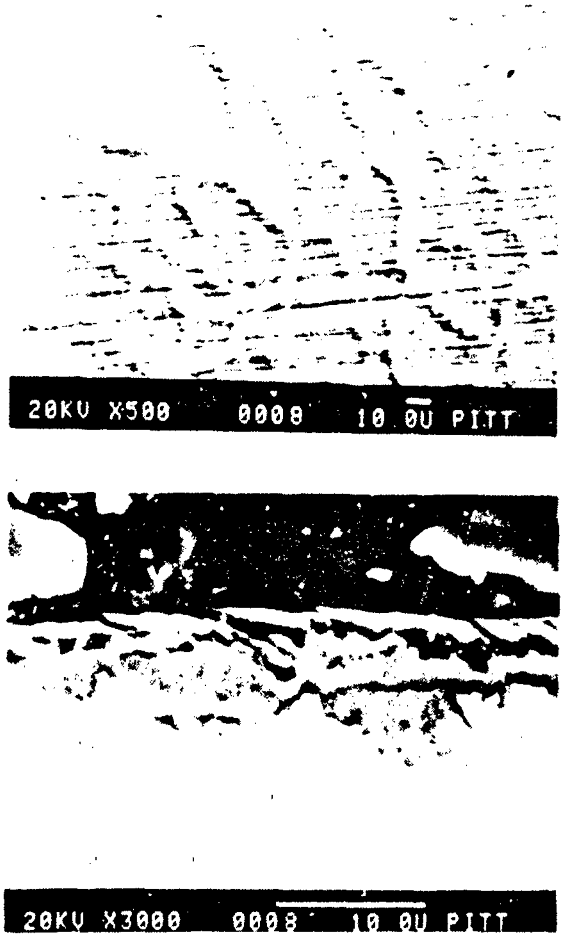

Figure 24. Surface (top) and cross-section (bottom) of $NbAl_3$ after 24 hrs. oxidation at 950°C indicating preferential attack of Nb_2Al at grain boundaries.

Niobium Aluminide

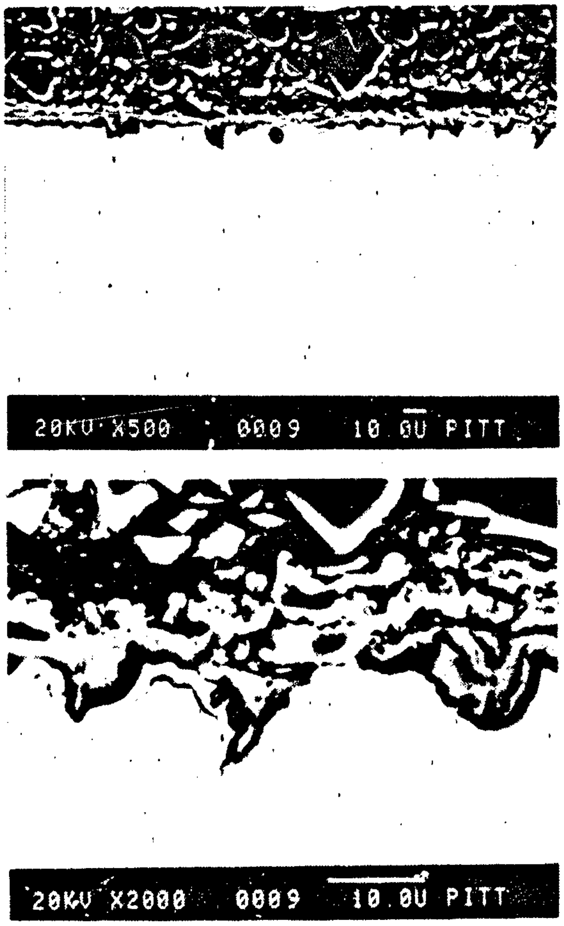

Figure 25. Secondary electron image of the cross-section of NbAl$_3$ after 24 hrs. oxidation at 1100°C (top) showing preferential attack of Nb$_2$Al at grain boundaries. Backscattered electron image showing alumina between an outer NbAlO$_4$ and inner Nb$_2$Al layer.

$NbAl_3$ 168hr Oxygen 1100C

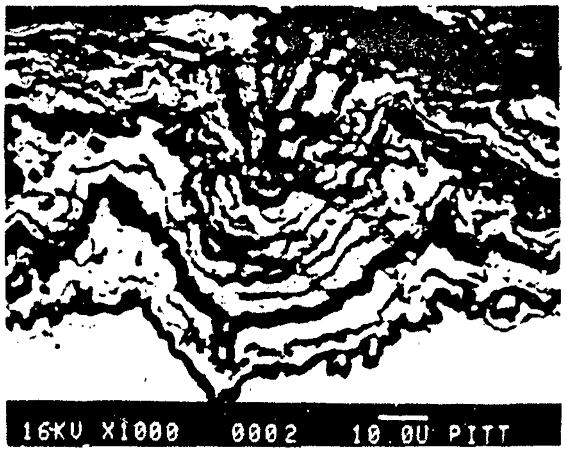

Black = Al_2O_3
Gray = $NbAlO_4$
White = Nb_2Al

Figure 26. Cross-section of $NbAl_3$ after 168 hrs. oxidation at 1100°C showing the development of a layered scale of Al_2O_3 and $NbAlO_4$.

Figure 27. Weight change vs time data for the oxidation of a series of Nb-base alloys in oxygen at 1100°C

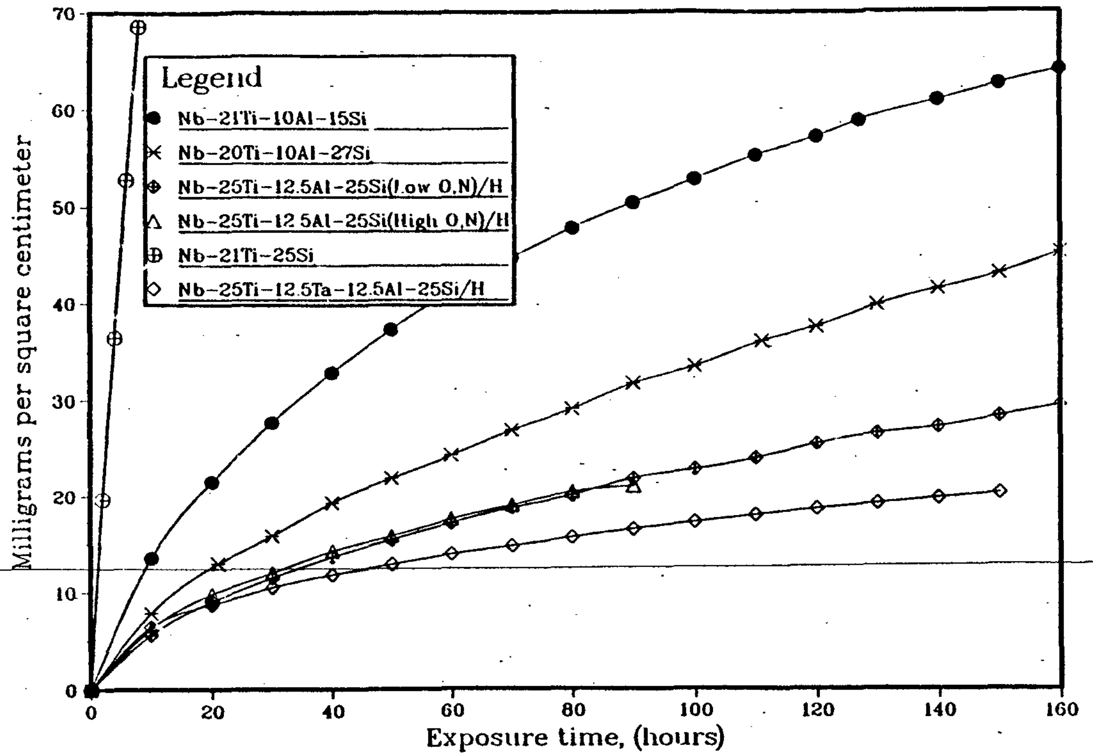

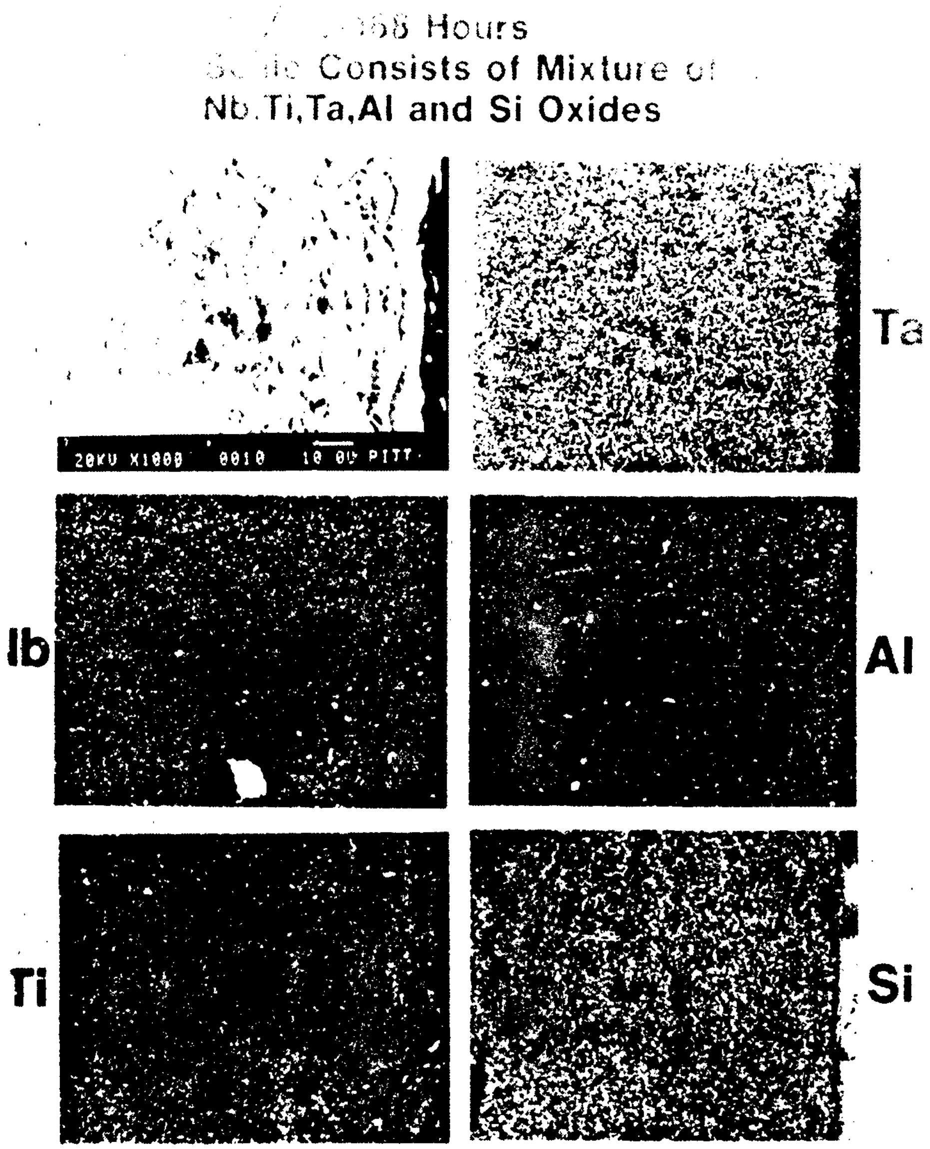

Figure 28. Cross-section of a Nb-Ti-Ta-Al-Si alloy after 168 hrs. oxidation at 1100°C and x-ray maps which indicate the various alloy components are oxidized in-situ.

The Effect of Microstructure on Oxidation

Nb-25Ti-12.5Al-25Si

Nb-25Ti-12.5Al-25Si/Hipped vs Nb-21Ti-10Al-15Si/Cast

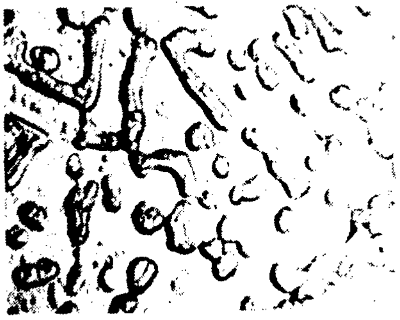

1000X **400X**

Starting Materials

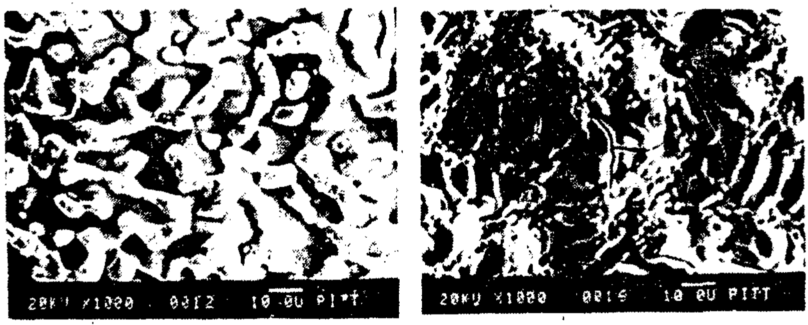

Oxidized / 1100°C - 168 Hours

Figure 29. Comparison of starting materials and structures following 168 hrs. oxidation at 1100°C for a Nb-Ti-Al-Si alloy which was prepared by casting and by hipping.

Microstructure of Tantalum Disilicide

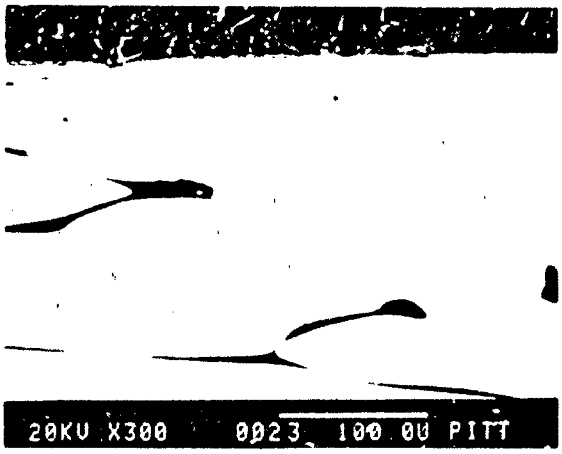

Figure 30. Initial microstructure of $TaSi_2$ (dark phase is elemental Si).

Figure 31. Weight change vs. time data for $TaSi_2$ and Al-modified $TaSi_2$ oxidized in oxygen at 800 and 1100°C.

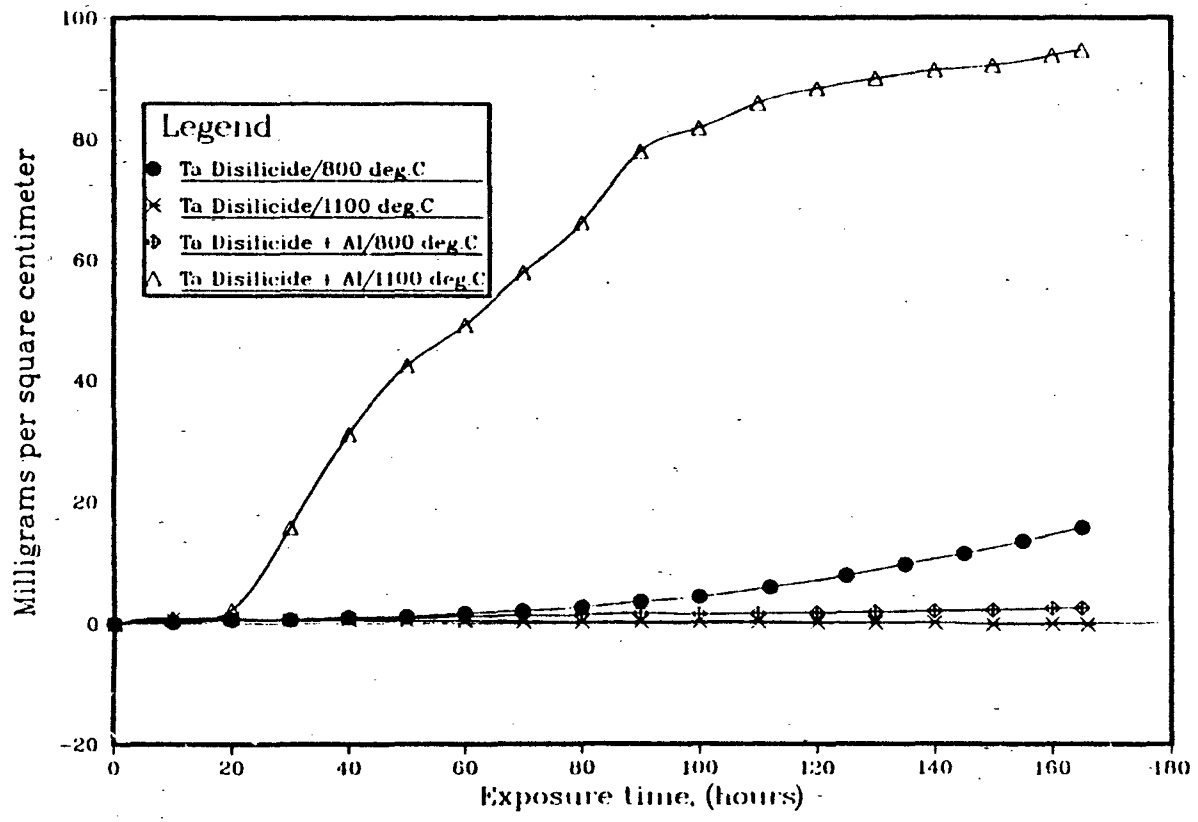

ium Disili

800°C-168 Hours

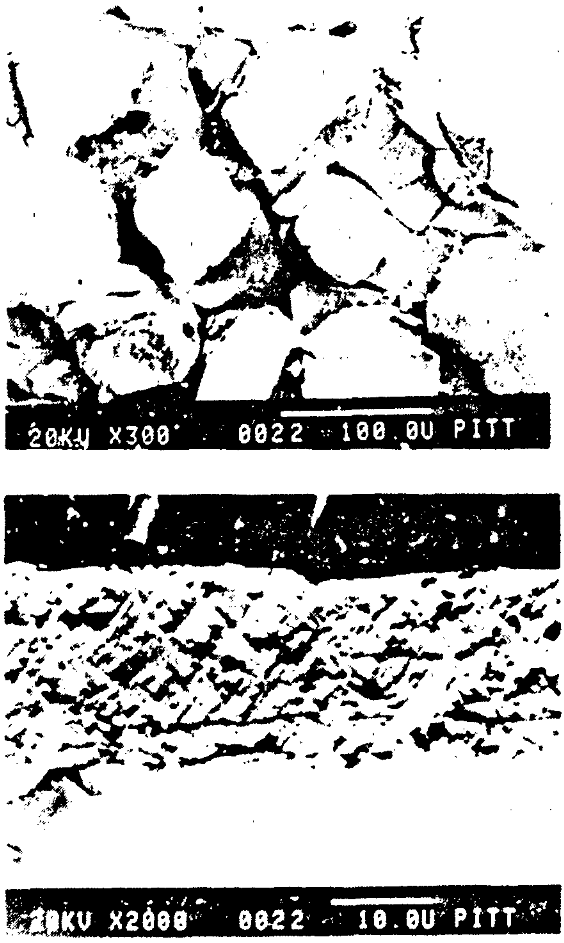

Figure 32. Surface (top) and cross-section (bottom) of $TaSi_2$ after 168 hrs oxidation at 800°C. The lighter phase is Ta_2O_5 and the dark phase is SiO_2.

Tantalum Disilicide

1100° C-168 Hours
Silica Layer(top)-Ta/Si oxides (bottom)

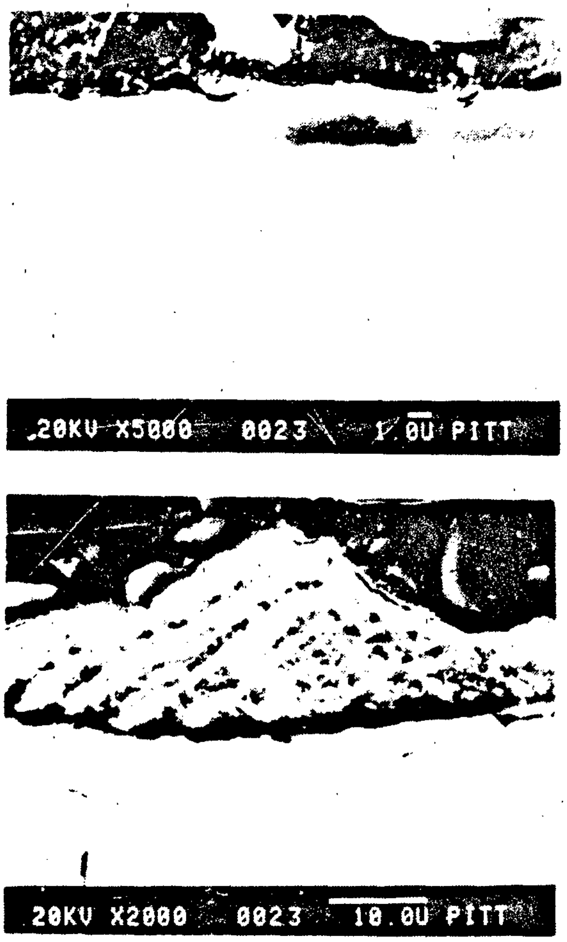

Figure 33. Cross-sections of TaSi$_2$ oxidized 168 hrs. at 1100°C showing exclusive formation of a silica film over some areas (top) and Ta-rich nodules over others (bottom).

Microstructure of Molybdenum Disilicide

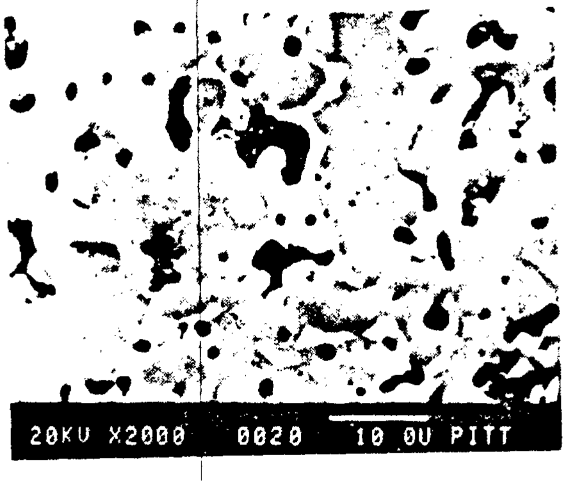

Figure 34. Initial microstructure of "$MoSi_2$". (White phase is Mo_5Si_3 and the dark phase is SiO_2). Th was detected adjacent to the silica regions.

Figure 35. Weight change vs. time data for $MoSi_2$ oxidized in oxygen at 600, 800, and 1100°C.

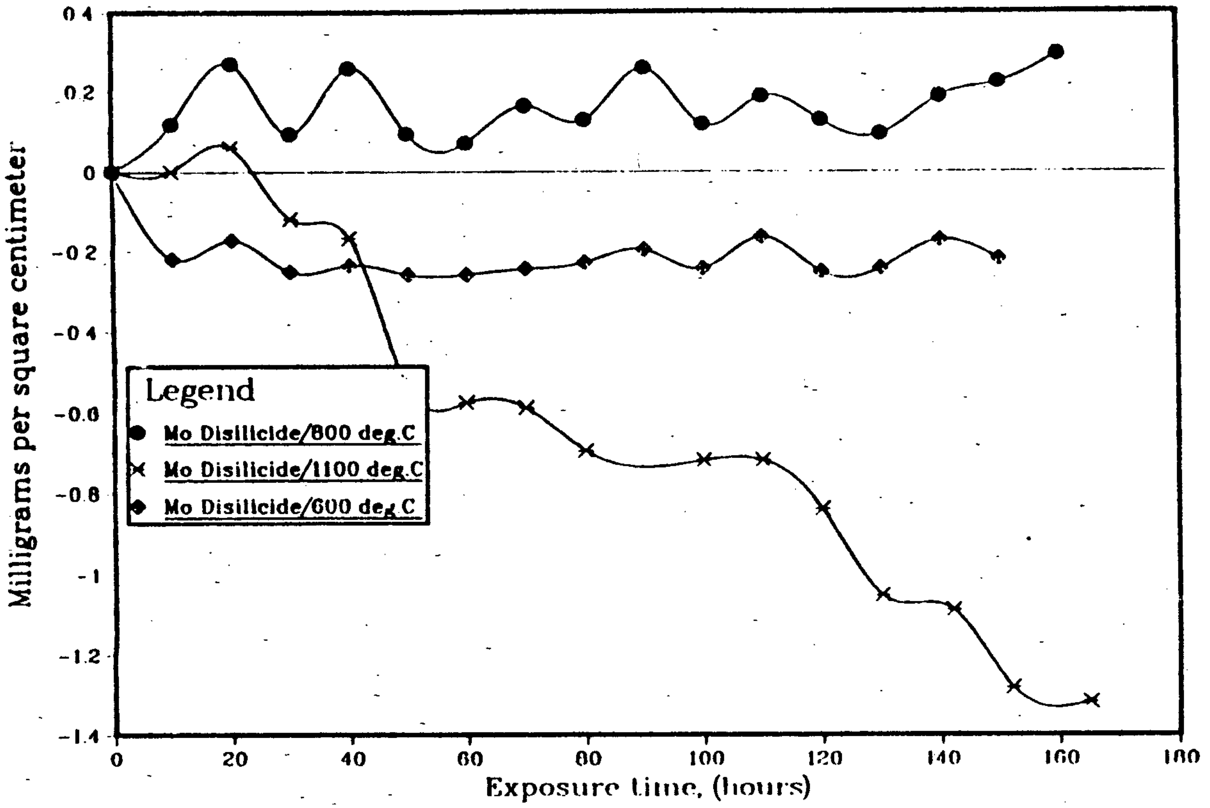

[illegible] silicide
[illegible] 1100 C
[illegible] Formation of Volatile Mo Oxides [illegible]

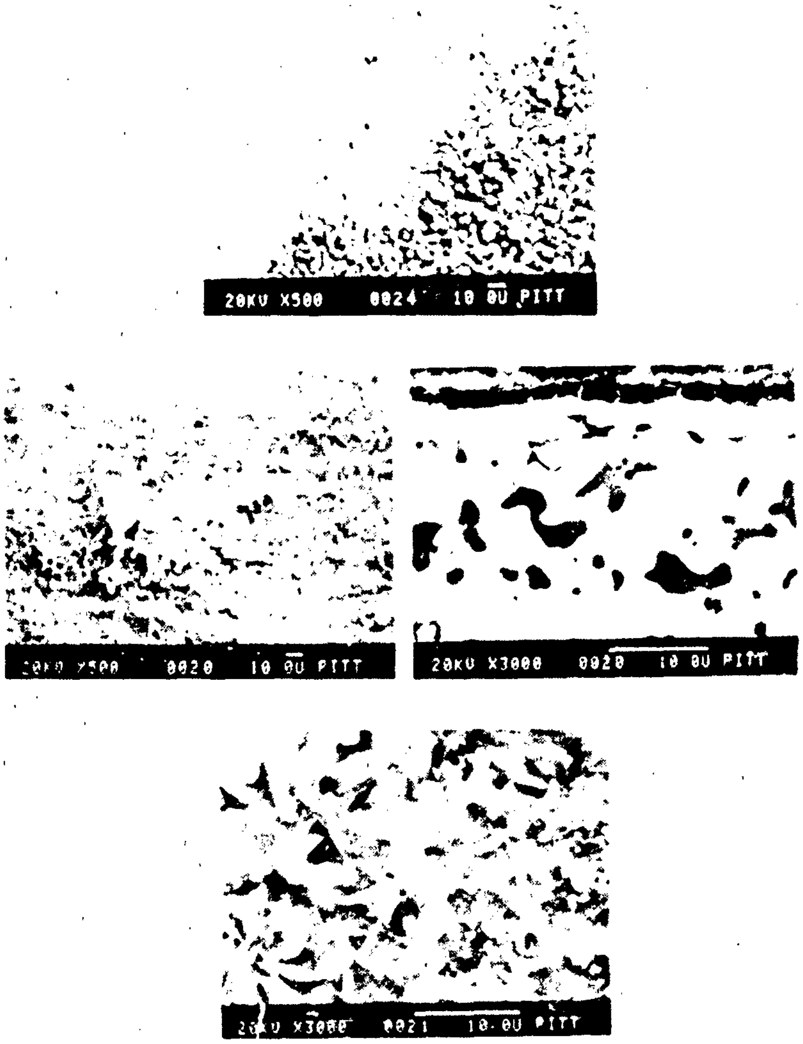

Figure 36. Top: Surface of $MoSi_2$ after 168 hrs. oxidation at 600°C.
Center: Surface(left) and cross-section(right) of $MoSi_2$ after 168 hrs. oxidation at 800°C.
Bottom: Surface of $MoSi_2$ after 168 hrs. oxidation at 1100°C.

PART II

STUDIES OF HYDROGEN EFFECTS IN Nb ALLOYS AND SELECTED INTERMETALLIC COMPOUNDS

by

A. W. Thompson and J. C. Williams

Department of Metallurgical Engineering and Materials Science
Carnegie Mellon University

ANNUAL REPORT

Nov. 1, 1987 - Oct. 30, 1988

Carnegie Mellon University
A.W. Thompson and J.C. Williams, Investigators

Initial work on hydrogen effects was focused on the titanium aluminide alloy Ti-24-11 (24% Al, 11%Nb in atom per cent), because of its availability, metallurgical knowledge, and technical interest for near-term aerospace applications. In addition, it contains very small amounts of beta phase in many accessible microstructures, making it essentially a single-phase aluminide alloy with the alpha-2 structure. Electrolytic and thermal methods for introducing hydrogen were developed, and measurements were made of the equilibrium solvi for various overpressures of hydrogen, over the temperature range 400 to 675°C. This is illustrated in Figure 1.

The alloy dissolves large amounts of hydrogen at elevated temperature, e.g. about 10% (atomic) near 600°C, but extrapolating the solvus to room temperature implies a solubility of around 1 ppm. Accordingly, cooling of charged material causes pronounced hydride formation. X-ray diffraction was used to determine that the hydride has the same fluorite structure as does TiH_2, although we do not know the stoichiometry of the hydride in Ti-24-11. These tests required a thorough investigation of heat-treatment response from hydrogen charging. Hydrogen is a potent stabilizer of the beta phase in titanium alloys, and particularly when amounts of the order of 10% (atomic) are charged, acts as a significant alloying element. The solvus measurements, heats of solution and partial molar free energies for hydrogen, and other related observations have been collected into a paper, entitled "Hydrogen Solubility in a Titanium Aluminide Alloy" and co-authored by W.-Y. Chu, A.W. Thompson and J.C. Williams, which is being submitted for publication. A summary of the same results was presented at the 2nd NASP Workshop on Hydrogen-Materials Interaction (Scottsdale, AZ, June 1-3) and was published in the Summary Proceedings of the workshop, Report NASP WP-1004, edited by H.G. Nelson (Nov. 1988).

Mechanical properties of the Ti-24-11 alloy have also been studied. The first part of the mechanical investigation comprised tensile tests using a range of strain rates and performed at several temperatures in the range -200°C to 400°C. Uncharged specimens as well as specimens thermally charged to four hydrogen contents between 500 and 2500 ppm by weight (2.5 -12.5% atomic) were tested under the conditions mentioned. Among the results were observation of a range in tensile ductilities, from 0.5 to 2.5%, and a pronounced strain rate effect, with an extremely steep fall in ductility for tests at rates above about 0.01 s^{-1}. This was true both with and without hydrogen, although the introduction of hydrogen lowered the critical rate somewhat, in addition to decreasing the stress and strain associated with fracture. This rate effect essentially represents the intervention of fracture in the stress-strain curve prior to yield, since no such rate effect could be detected when compression tests were conducted under otherwise identical conditions. The dependence of tensile properties on temperature and hydrogen content, respectively, are shown in Figures 2 and 3.

To facilitate study of the brittle fracture process in Ti-24-11, notched bend bar specimens were also tested, under parallel conditions to those mentioned for the tensile tests. Generally, very similar phenomena were observed, including the pronounced strain rate effect. Using established analysis methods, it was possible from these tests to calculate the true, intrinsic fracture strength for cleavage of the specimens. This strength was found to be independent of temperature, in agreement with the classical expectation, but was sensitive to crosshead speed in the same manner as the nominal fracture stress. The fracture strength also decreased with addition of hydrogen.

Fractographic examination revealed that fracture in tension or bend bars took place by a cleavage-like process in small facet-like features. The size and shape of these features corresponded accurately to the plates of alpha-2 in the microstructure. The fracture process thus appears to be one of tearing in the "matrix" of transformed beta around the primary alpha-2 plates, and a brittle fracture of cleavage-like appearance in the plates themselves. Similar observations have been made in other titanium alloys and in certain microstructures of titanium aluminides.

The bend-bar experiments showed that propagation of cleavage cracks appeared to take place in a stable manner during slow loading, and resistance to this slow propagation was dependent on crosshead speed and hydrogen content. Accordingly, additional tests were conducted with pre-cracked WOL (wedge-opening loading) specimens to permit measurement of conventional toughness properties as well as crack propagation resistance. Toughness, as measured by K_{Ic}, and the threshold stress for cracking in hydrogen, K_{IH}, were both found to decrease smoothly with increasing hydrogen content, in tests using fracture mechanics specimens (compact tension or WOL). These data, together with the fracture strength measured in bend bars, are collected in Figure 4. Although the toughness does decrease considerably (as do tensile properties in Fig. 3), it should be noted that the hydrogen contents are very large, compared to damaging amounts in a number of other materials, including steels and nickel-base alloys. Thus Figs. 3 and 4 could be interpreted as showing that Ti-24-11 actually is a relatively hydrogen-tolerant alloy.

Crack growth curves, measured as da/dt in sustained loading, as a function of the crack driving force, K_I, are shown in Figure 5. The threshold stress (see Fig. 4) falls steadily with the increase of hydrogen content, but note that the curves remain "rounded" at growth rates above 1 micrometer per minute. Thus the cracking resistance remains considerable at even the highest hydrogen content. Conventional crack resistance curves, or R curves, are being developed to express this result.

The mechanical properties work in this program has now been summarized in two papers, which will be submitted shortly to appropriate journals. These are entitled "Brittle Fracture and Behavior of Hydrides in Ti-24 Al-11 Nb", and "Hydrogen-induced Crack Growth in Ti-24 Al-11 Nb". Each is authored by W. -Y.Chu and A.W. Thompson.

In the past quarter, we have investigated the effect of microstructure differences on mechanical properties of Ti-24-11, as a function of hydrogen content. Particular emphasis has been placed on measurement of the intrinsic cleavage fracture strength. In earlier work on this program, it was found that changing microstructure through changes in solutionizing temperature and cooling rate from that temperature could result in variations in yield strength, fracture strain, and cleavage fracture strength of 20-30%, compared to as-received material. However, we have now found that the yield strength, fracture strain and cleavage fracture strength all increased by 50-100% when solution treatment was conducted in hydrogen gas (instead of vacuum), at solution temperatures of 1100°C and above, followed by aging at 800°C. If the cooling rate was low, e.g. furnace cooling or controlled cooling, or if the solution temperature was below 1100°C,, e.g. 1000°C or 1075°C, solution treatment in hydrogen gas then caused an increase in the yield strength, fracture strain and cleavage fracture strength by only 10-20%.

For any of these microstructures, the ultimate strength, the fracture strain and the cleavage fracture strength decreased steeply when the crosshead speed was larger than 50 mm/min. At speeds this high, the difference between solution treatment in hydrogen gas or in vacuum was slight.

For these experiments, hydrogen can be regarded as a temporary alloying element, stabilizing the beta phase during heat treatment, and perhaps also affecting elevated temperature mechanical properties and the corresponding accommodation response within the microstructure, during subsequent transformations. This was indicated metallographically in these specimens by increased size of the microstructural constituents, and modest increases in volume fraction of beta phase, as a result of solution treatment in hydrogen.

For the next period, we plan to investigate the effect of microstructural variation and hydrogen content (resulting from hydrogen solution treatment) on the fracture toughness, crack propagation rate, and threshold stress intensity for hydrogen-induced cracking. We are optimistic that the improved mechanical properties seen in tensile tests will be reflected in improved toughness and cracking resistance properties.

Dr. J.C. Williams left Carnegie Mellon University in August, 1988, to join the Aircraft Engine Business Group of General Electric in Evendale, Ohio. Professor Thompson now acts as the sole investigator in the CMU portion of this program.

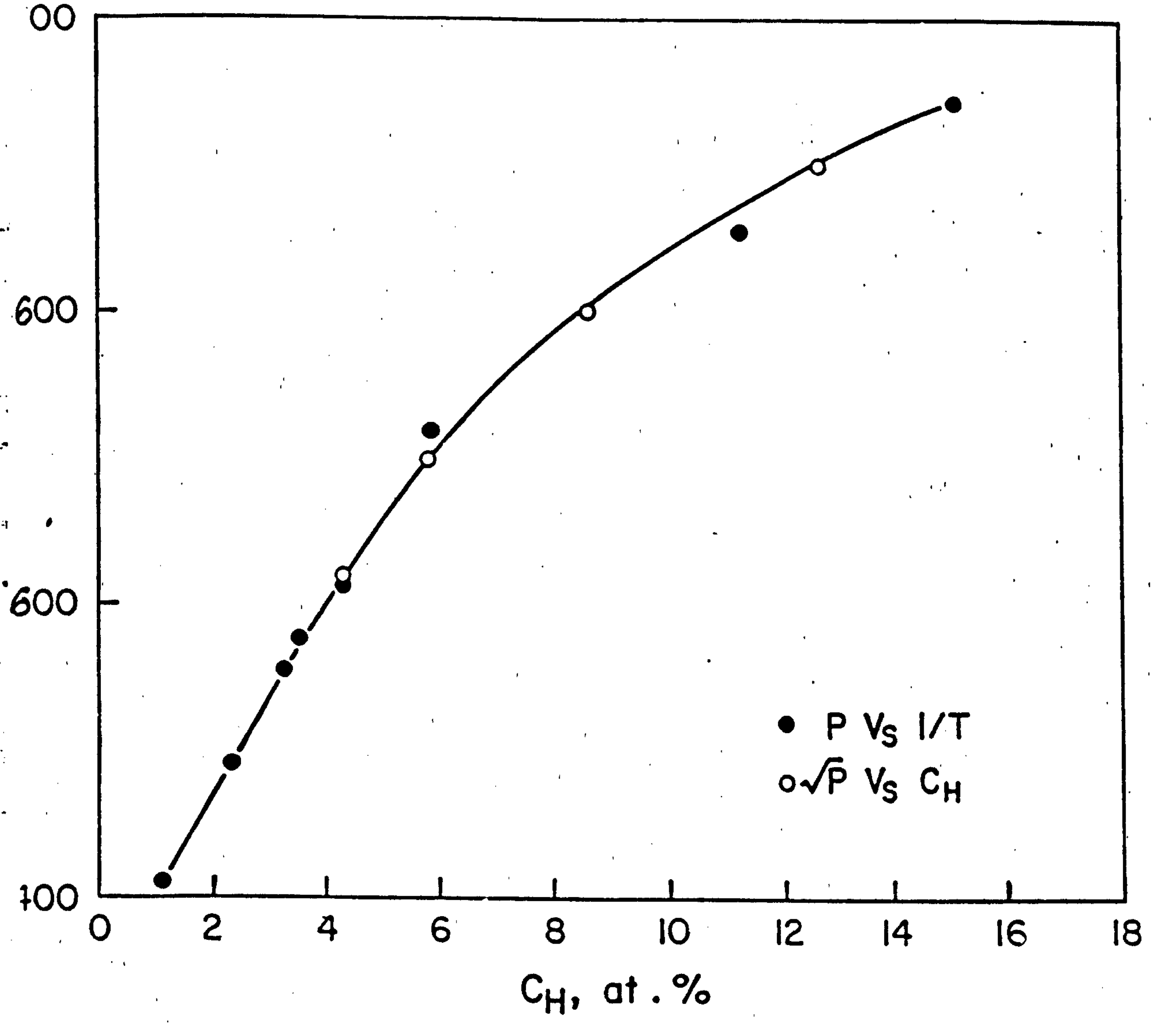

Figure 1. Solvus for hydrogen in Ti-24-11 in equilibrium with hydride phase, as determined by two methods (shown in figure).

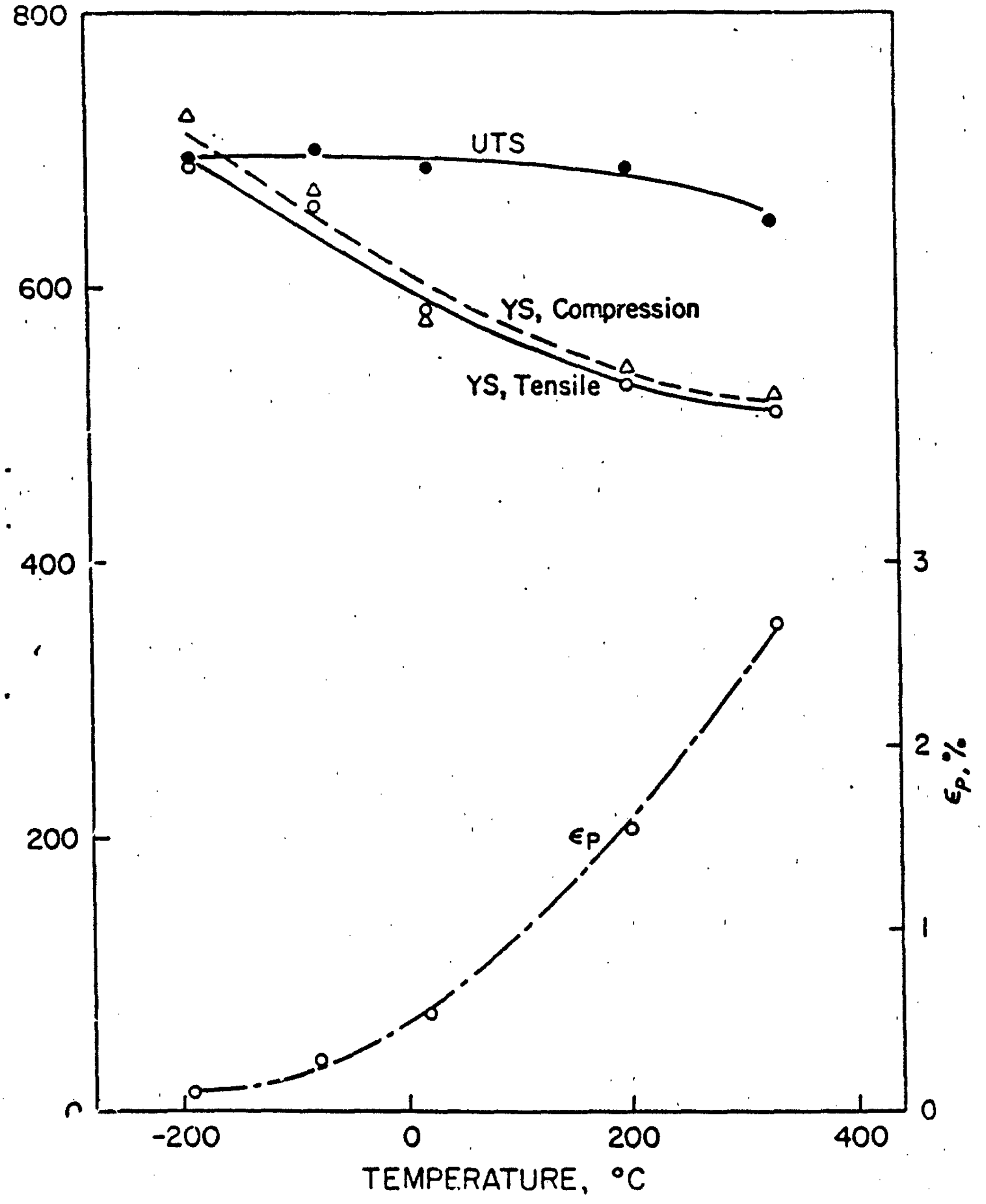

Figure 2. Mechanical properties of Ti-24-11 as a function of temperature, in the absence of hydrogen. Note that compression and tension yield strengths are closely parallel for the no-hydrogen material.

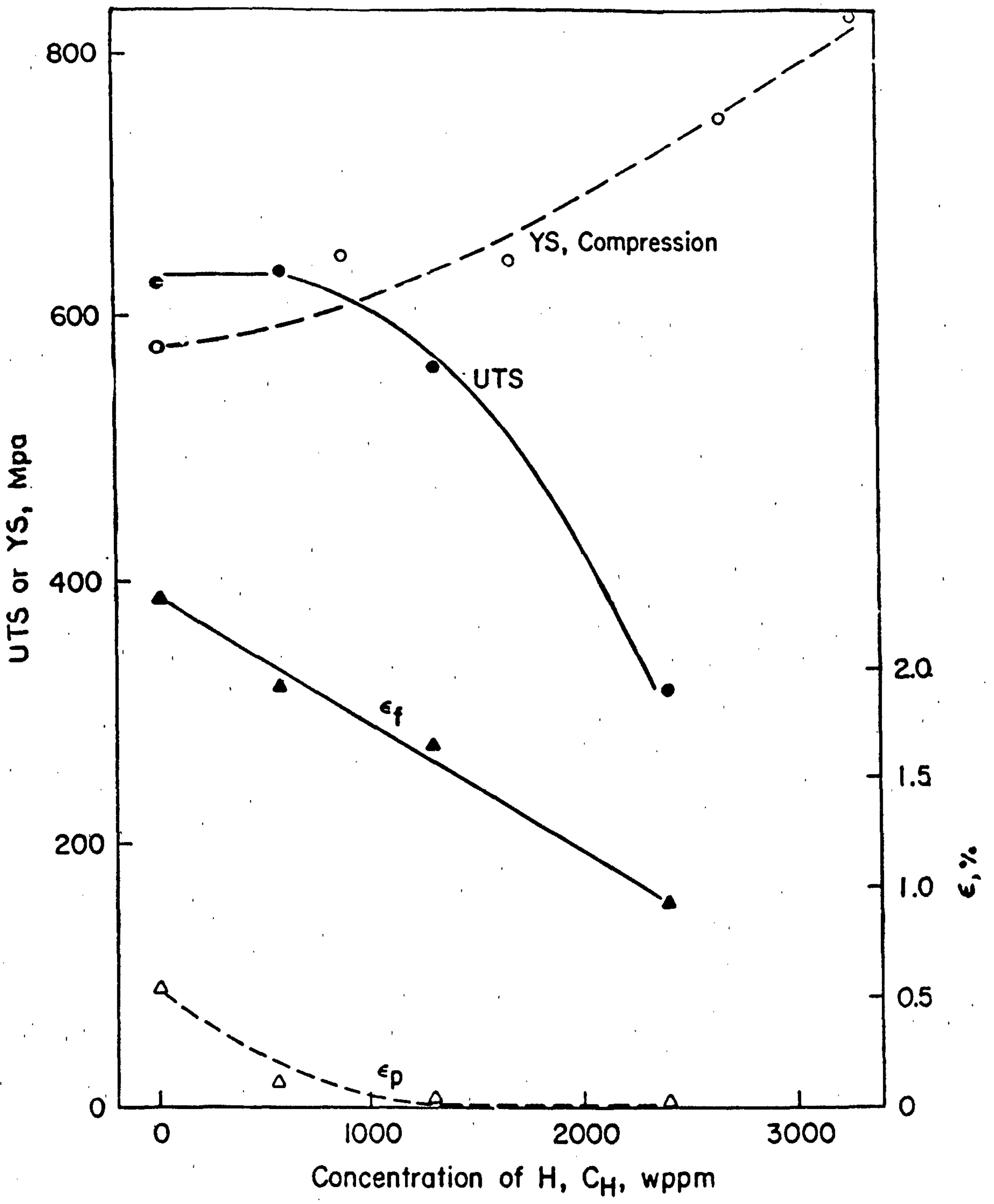

Figure 3. Mechanical properties of Ti-24-11 as a function of precharged hydrogen content. Note that above about 1000 wppm hydrogen, fracture occurs prior to yield, so that the apparent UTS becomes smaller than the compressive YS.

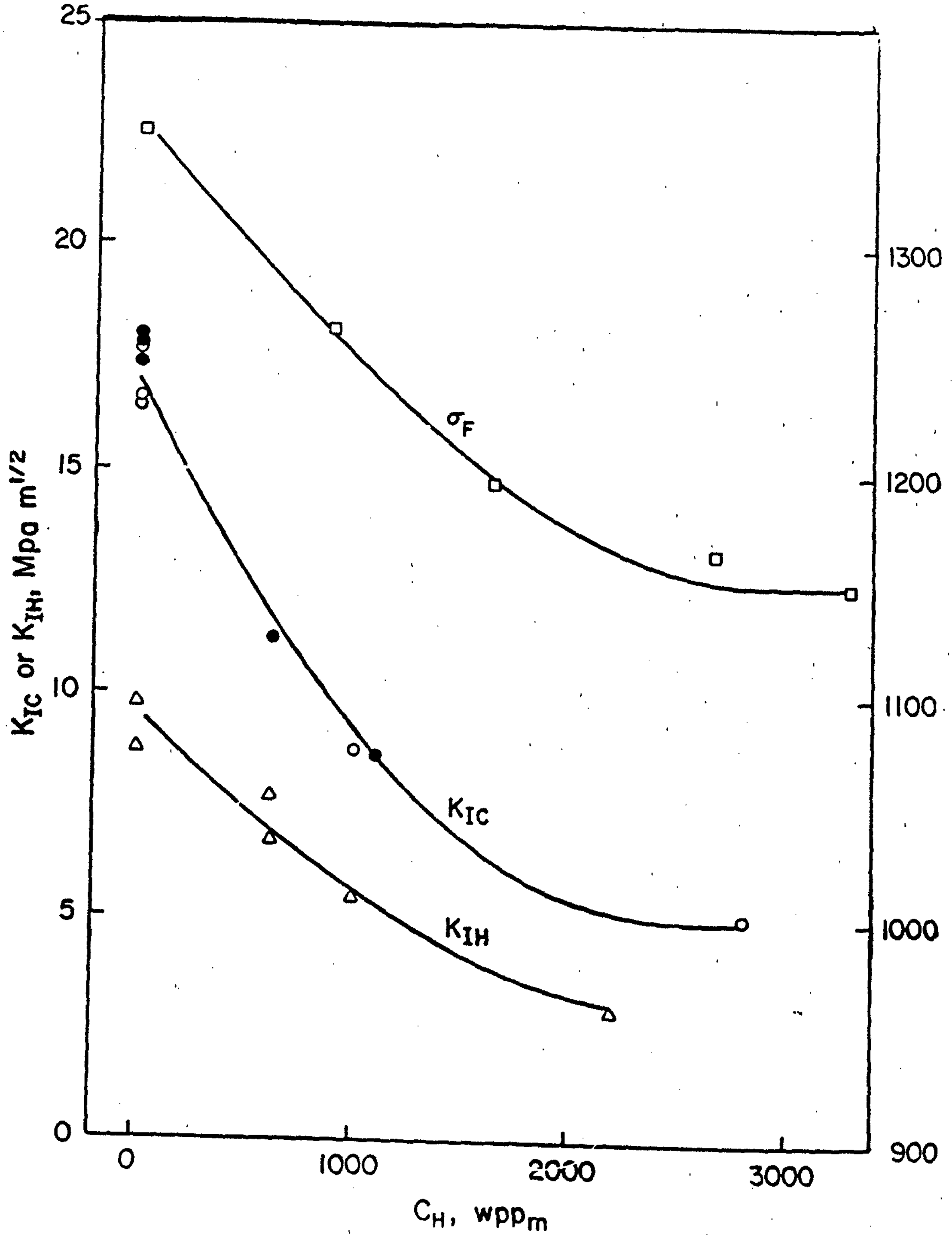

Figure 4. Fracture toughness, K_{Ic}, cracking threshold, K_{IH}, and fracture strength in bend bars, as functions of precharged hydrogen content.

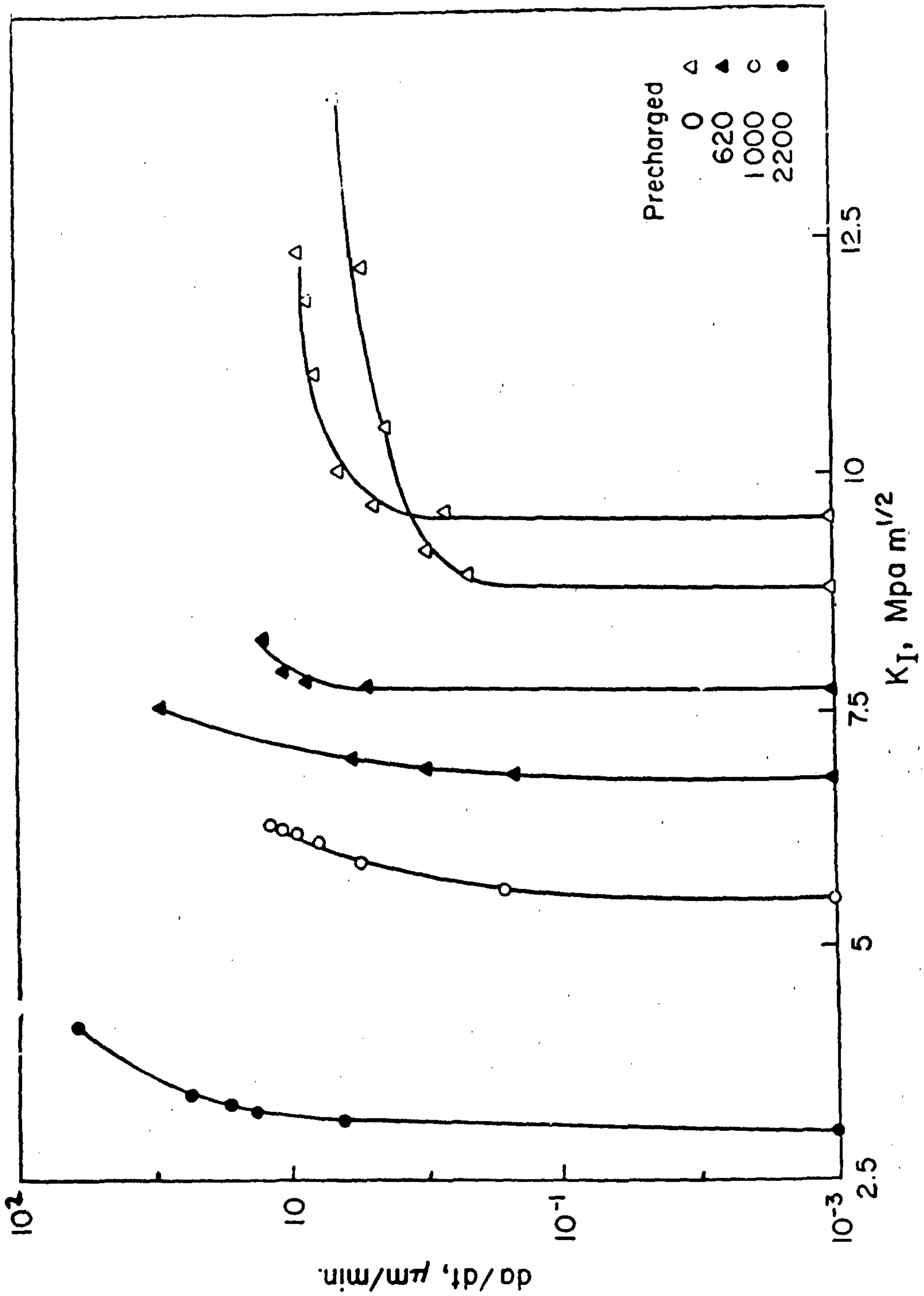

Figure 5. Crack growth rate, da/dt (crack length = a) as a function of crack driving force, K_I, for uncharged Ti-24-11 and for specimens with three precharged hydrogen contents (shown).